



Lukas Ladenstein, BSc

# From Tetragonal to Cubic – Searching for New Highly Conducting Li-oxide Garnets

---

## MASTERARBEIT

zur Erlangung des akademischen Grades  
Diplom-Ingenieur  
Masterstudium Technical Chemistry

eingereicht an der  
**Technischen Universität Graz**

Betreuer:  
Dr.techn. Daniel Rettenwander  
Univ.-Prof. Dr.rer.nat. Martin Wilkening

Institut für Chemische Technologie von Materialien

Graz, Oktober 2018

## **EIDESSTATTLICHE ERKLÄRUNG**

Ich erkläre an Eides statt, dass ich die vorliegende Arbeit selbstständig verfasst, andere als die angegebenen Quellen/Hilfsmittel nicht benutzt, und die den benutzten Quellen wörtlich und inhaltlich entnommenen Stellen als solche kenntlich gemacht habe. Das in TUGRAZ online beziehungsweise UNIGRAZ online hochgeladene Textdokument ist mit der vorliegenden Diplomarbeit ident.

## **STATUTORY DECLARATION**

I declare that I have authored this thesis independently, that I have not used other than the declared sources / resources, and that I have explicitly marked all material which has been quoted either literally or by content from the used sources. The text document uploaded on TUGRAZ online and UNIGRAZ online is identical to the present diploma thesis.

---

Graz, date

---

Lukas Ladenstein

# Acknowledgement

First, I would like to thank Univ.-Prof. Dr.rer.nat. Martin Wilkening for giving me the opportunity to work on my diploma thesis in the Institute for Chemistry and Technology of Materials. Furthermore, I would like to acknowledge the Christian-Doppler Laboratory for Lithium-Ion Batteries for the financial support.

A special thanks to Dr.techn. Daniel Rettenwander for providing me the topic, for the great support and for being such a good mentor during the whole time I was working on my diploma thesis.

I would also like to thank Maria Gombotz for helping me with the interpretation of the results, setting up the measurements and for always having time if I needed her expertise.

Further, to the whole working group for the good working atmosphere and any kind of help.

I also want to acknowledge Dipl.-Ing Dr.techn. Brigitte Bitschnau and Ao.Univ.-Prof. Dipl.-Ing. Dr.techn. Franz-Andreas Mautner for the X-ray measurements.

Additionally, I want to thank my colleagues Katharina and, in particular, Florian, who became one of my closest friends and faithful companions over the last years of studying and especially during the time I was working on my diploma thesis.

Finally, I would like to thank my parents for the support over the last few years, which made this thesis even possible in the first place and to Elisabeth for the encouragement since we first met.

# Abstract

Energy storage is one of the most important issues to successfully achieve the change from fossil fuels to renewable resources. Due to the constantly increasing population the demand for energy rises, making it inevitable to search for new technologies for storing energy. Thus, Li-ion conductors gained much importance over the last years as they are found in many electrochemical devices. Still, this field of study is yet not completely understood making it necessary to find new materials.

In this diploma thesis, the main focus is on the Li-oxides  $\text{Li}_{7-x}\text{La}_3\text{Hf}_{2-x}\text{Ta}_x\text{O}_{12}$  and  $\text{Li}_{7-x}\text{La}_3\text{Sn}_{2-x}\text{Ta}_x\text{O}_{12}$  with varying stoichiometry, showing garnet-type structure in tetragonal and cubic modification. It was tried to stabilize the cubic modification and to find the best composition in respect to the ionic conductivity and activation energy. Solid state synthesis in combination with high-energy ball milling was performed for the synthesis of the materials. X-ray diffraction measurements were performed for the optimization of the synthesis route and to determine the crystal structure. Differential thermal analysis coupled with thermogravimetry was carried out to determine phase transitions in the sintering process. Finally, electrochemical impedance spectroscopy measurements were performed to determine dielectric properties.

# Kurzfassung

Energiespeicherung ist eines der wichtigsten Themen um den Wandel von fossilen Treibstoffen zu erneuerbaren Energien zu ermöglichen. Aufgrund der Tatsache, dass der Energiebedarf durch eine immer weiter steigende Weltbevölkerung stetig zunimmt, ist es dringend erforderlich, nach neuen Technologien zur Speicherung von Energie zu suchen. Aus diesem Grund haben Li-Ionen-Leiter in den letzten Jahren stark an Wichtigkeit zugenommen, weshalb sie bereits jetzt in vielen elektronischen Geräten eingebaut und in Verwendung sind. Allerdings gibt es immer noch einige Schwierigkeiten, weshalb es notwendig ist, nach weiteren, neuen Materialien mit verbesserten Eigenschaften zu suchen.

Im Rahmen dieser Diplomarbeit liegt das Hauptaugenmerk auf den beiden Li-Oxiden  $\text{Li}_{7-x}\text{La}_3\text{Hf}_{2-x}\text{Ta}_x\text{O}_{12}$  und  $\text{Li}_{7-x}\text{La}_3\text{Sn}_{2-x}\text{Ta}_x\text{O}_{12}$ , welche unterschiedliche Stöchiometrie aufweisen. Des Weiteren besitzen sie eine granatähnliche Struktur, welche je nach Zusammensetzung und Behandlung in tetragonaler und kubischer Kristallstruktur vorliegt. Es wurde versucht die kubische Struktur zu stabilisieren und in Abhängigkeit von der Leitfähigkeit und der Aktivierungsenergie die beste Zusammensetzung zu finden. Dafür wurde eine Kombination aus Festkörpersynthese mit Hochenergie-Mahlen verwendet und anschließend mit Röntgendiffraktometrie eine Optimierung der Syntheseschritte vorgenommen sowie die Kristallstruktur der jeweiligen Materialien bestimmt. Um Phasenübergänge während des Sinterschrittes bestimmen zu können, wurde eine Differenz-Thermoanalyse mit gekoppelter Thermogravimetrie der jeweiligen undotierten Granate durchgeführt. Anschließend wurden mittels elektrochemischer Impedanzspektroskopie dielektrische Eigenschaften der Materialien ermittelt.

# Content

Acknowledgement .....	I
Abstract .....	II
Kurzfassung .....	III
<b>1. Introduction .....</b>	<b>1</b>
1.1. Motivation .....	1
1.2. Li-oxide Garnets – A Short Overview .....	2
<b>2. General Aspects .....</b>	<b>6</b>
2.1. Diffusion in Solids .....	6
2.1.1. <i>Mass Transport</i> .....	6
2.1.2. <i>Inter-atomic Diffusion Processes</i> .....	8
2.1.3. <i>Defects</i> .....	10
2.2. X-Ray Diffraction .....	11
2.2.1. <i>Miller Indices</i> .....	12
2.2.2. <i>Laue Equation</i> .....	12
2.2.3. <i>Bragg Equation</i> .....	13
2.3. Impedance Spectroscopy .....	14
2.3.1. <i>Impedance</i> .....	14
2.3.2. <i>Conductivity Isotherms</i> .....	16
2.3.3. <i>Nyquist Plot</i> .....	17
<b>3. Experimental .....</b>	<b>20</b>
3.1. $\text{Li}_{7-x}\text{La}_3\text{Hf}_{2-x}\text{Ta}_x\text{O}_{12}$ (Ta-LLHO) .....	20
3.2. $\text{Li}_{7-x}\text{La}_3\text{Sn}_{2-x}\text{Ta}_x\text{O}_{12}$ (Ta-LLSO) .....	24
3.3. Characterization .....	25
<b>4. Results .....</b>	<b>26</b>
4.1. $\text{Li}_{7-x}\text{La}_3\text{Hf}_{2-x}\text{Ta}_x\text{O}_{12}$ (Ta-LLHO) .....	26
4.1.1. <i>Differential Thermal Analysis Coupled with Thermogravimetry</i> .....	26
4.1.2. <i>X-Ray Diffraction</i> .....	27

4.1.3.	<i>Dimensional Change after Sintering</i> .....	31
4.1.4.	<i>Electrical Studies</i> .....	33
4.2.	$\text{Li}_{7-x}\text{La}_3\text{Sn}_2\text{Ta}_x\text{O}_{12}$ (Ta-LLSO).....	39
4.2.1.	<i>Differential Thermal Analysis Coupled with Thermogravimetry</i> .....	39
4.2.2.	<i>X-Ray Diffraction</i> .....	40
4.2.3.	<i>Dimensional Change after Sintering</i> .....	44
4.2.4.	<i>Electrical Studies</i> .....	46
4.3.	Discussion.....	50
4.3.1.	<i>Crystal Structure</i> .....	50
4.3.2.	<i>Electrochemical Studies</i> .....	51
<b>5.</b>	<b>Conclusion</b> .....	<b>53</b>
	<b>Bibliography</b> .....	<b>54</b>
	<b>List of Figures</b> .....	<b>57</b>
	<b>List of Tables</b> .....	<b>60</b>

# List of Abbreviations

AC	Alternating current
DC	Direct current
e.g.	For example
DTA	Differential thermal analysis
DTA-TG	Differential thermal analysis coupled with thermogravimetry
EIS	Electrochemical impedance spectroscopy
fcc	Face centered cubic
h	Hour(s)
LIB	Li ion battery
LLHO	$\text{Li}_7\text{La}_3\text{Hf}_2\text{O}_{12}$
LLSO	$\text{Li}_7\text{La}_3\text{Sn}_2\text{O}_{12}$
LLTO	$\text{Li}_7\text{La}_3\text{Ta}_2\text{O}_{12}$
LLZO	$\text{Li}_7\text{La}_3\text{Zr}_2\text{O}_{12}$
min	Minute(s)
pfu	Per formula unit
PXRD	Powder X-ray diffraction
rpm	Rounds per minute
s	Second(s)
SG	Space group
SHE	Standard hydrogen electrode
Ta-LLHO	$\text{Li}_{7-x}\text{La}_3\text{Hf}_{2-x}\text{Ta}_x\text{O}_{12}$
Ta-LLSO	$\text{Li}_{7-x}\text{La}_3\text{Sn}_{2-x}\text{Ta}_x\text{O}_{12}$
TGA	Thermogravimetric analysis
vs.	Versus

# List of Symbols

C	Concentration
d	Interplanar spacing
D	Diffusion coefficient
E	Voltage
$E_A$	Activation energy
$E_m$	Barrier energy
$G_m$	Gibbs free enthalpy of migration
$H_m$	Enthalpy of migration
I	Current
J	Diffusion Flux
K	Prefactor
$k_B$	Boltzmann constant
n	Order of reflection
R	Resistance
$S_m$	Entropy of migration
t	Time
T	Temperature
Z	Impedance
a,b,c	Unit cell parameters
x,y,z	Miller indices
$\Gamma$	Jump rate of vacancies
$\Delta$	Laplace operator
$\lambda$	Wavelength
$\rho$	Density
$\sigma$	Conductivity
$\phi$	Phase shift
$\omega$	Radial frequency
$\nabla$	Vector operation divergence

# 1. Introduction

## 1.1. Motivation

Energy storage is one of the most important issues to successfully achieve the change from fossil fuels to renewable resources, because fossil fuels are limited and will one day no longer be available. On the other hand, a steady growth of the world population will increase the need of more energy. Prognoses say that the population on our planet will rise to 9.7 billion people in 2050 and to 11.2 billion in 2100. [1] This trend makes it inevitable to search for new technologies to cover the need for energy. One technology that is part of the energy revolution was found in solar cells, which convert solar radiation to usable energy, and wind energy, respectively. The problem with those technologies is that the production of energy is only possible if sun or wind is available. To be able to store the energy that is produced, rechargeable batteries are inevitable. These are just two examples of various applications in which energy needs to be stored. [2] In this case, Li-ion batteries (LIBs) gained high interest over the last years due to their good electrical properties. [3]

Still, this field of study is yet not completely understood and lots of problems have yet not been solved regarding different properties of the batteries used. For fully functioning LIBs, a high mechanical and chemical stability has to be given. Furthermore, it is necessary that batteries show long lifetimes over many charge- and discharge cycles and high capacities need to be given. There are already batteries used in our daily lives, which fulfill most of these requirements by using liquid electrolytes. In some concepts, Li metal is used as the anode material in, for example (e.g.) Li/sulfur or Li/air batteries. In redox flow batteries, low density of  $0.59 \text{ g}\cdot\text{cm}^{-3}$  and high theoretical specific capacities of  $3860 \text{ mA}\cdot\text{h}^{-1}$  are possible, while it shows the lowest negative chemical potential of  $-3.04 \text{ V}$  versus (vs.) the standard hydrogen electrode (SHE). Further, these batteries have a very good contact area with the electrodes and size changes of the electrodes show no problems while charging and discharging take place. However, many safety issues are yet not solved regarding the formation of Li dendrites in cells with liquid electrolytes. Because of those reasons, all-solid-state Li-ion batteries have gained much interest over the years in major as all solid state electrolytes in technological developments due to their high physical and chemical stability compared to liquid electrolytes. Furthermore, solid electrolytes show great stability against Li metal. This makes it possible to investigate batteries based on Li metal. [4],[5]

Li-ion conducting oxides are very promising and have been widely investigated in this field of study. One of the best results regarding a large electrochemical potential window and high thermal performance could be found for  $\text{Li}_7\text{La}_3\text{Zr}_2\text{O}_{12}$  (LLZO) that works as an electrolyte in

all-solid-state secondary batteries. At room temperature (RT), LLZO crystallizes in its low conductive tetragonal modification (space group (SG):  $I4_1/acd$ , No. 142). The highly conductive, high temperature cubic modification (SG:  $Ia\bar{3}d$ , No. 230) can be stabilized by supervalent doping of the Li, La or Zr site with e.g. Al or Ga with different stoichiometry, which provides a different Li-ion diffusion mechanism compared to tetragonal LLZO. However, there are many more Li metal oxides with garnet-type structure with tetragonal modification and the general chemical formula  $\text{Li}_7\text{La}_3\text{M}_2\text{O}_{12}$  ( $\text{M} = \text{Sn}, \text{Hf}, \dots$ ).

The question appeared if there are also other garnets that crystallize in the tetragonal modification and further if it is possible to stabilize the cubic phase of those garnets by supervalent doping. In this diploma thesis the focus lies on the synthesis of the tetragonal Li-oxides LLHO and LLSO and to stabilize their cubic polymorphs by doping with Ta in different stoichiometry according to the chemical formulas  $\text{Li}_{7-x}\text{La}_3\text{Hf}_{2-x}\text{Ta}_x\text{O}_{12}$  and  $\text{Li}_{7-x}\text{La}_3\text{Sn}_{2-x}\text{Ta}_x\text{O}_{12}$  such as in Ta doped LLZO. [6] Furthermore, the electric properties are analyzed and compared to cubic LLZO.

## 1.2. Li-oxide Garnets – A Short Overview

One type of complex oxides is garnets, which can be both minerals and synthetic materials. Due to their excellent physical and chemical properties, garnets are used for many different applications ranging from garnet paper for smoothing wood to being incorporated in electronic devices. Garnets are composed of various elements with the general chemical formula  $\text{A}_3\text{B}_2(\text{XO}_4)_3$  ( $\text{A} = \text{Ca}, \text{La}, \text{rare earth}, \dots$ ;  $\text{B} = \text{Al}, \text{Fe}, \text{Ge}, \dots$ ;  $\text{X} = \text{Si}, \text{Ge}, \text{Al}$ ), whereas the ionic size and the electronic configuration are of high importance. A, B and X are coordinated with eight, six and four oxygen atoms on their cation sites and show a face centered cubic (fcc) structure. [7] The occupation and the SG position in the crystal structure are given in Tab. 1.1.

Tab. 1.1: Description of the garnet structure. The reference is taken from [8].

<b>Point symmetry</b>	222	$\bar{3}$	$\bar{4}$	$\bar{1}$
<b>SG position</b>	24 c	16 a	24 d	96 h
<b>Typical ideal formula</b>	$\text{A}_3$	$\text{B}_2$	$\text{X}_3$	$\text{O}_{12}$
<b>Coordination to oxygen</b>	8	6	4	-
<b>Type polyhedron</b>	dodecahedron	octahedron	tetrahedron	-

One of the most important characteristics of garnets is that it is possible to synthesize Li-stuffed garnet materials. By increasing the amount of Li atoms in a unit cell to five, the synthesized materials start showing promising results regarding ionic conductivity (up to three orders of magnitude compared to Li-poor garnets) and good mechanical and thermal stability. This makes them to an interesting solid electrolyte for rechargeable LIBs. Since the first Li-stuffed garnet ( $\text{Li}_5\text{La}_3\text{M}_2\text{O}_{12}$  ( $\text{M} = \text{Hf}, \text{Nb}$ ) showing a conductivity  $\sigma$  of  $10^{-6} \text{ S}\cdot\text{cm}^{-1}$  at RT) was published by *Thangadurai et al.* in 2003, various Li-rich garnet-type materials with tetragonal and cubic crystal structure have been investigated in literature. [7],[9]

One of the most promising Li oxides with garnet-type structure contains up to seven Li atoms per unit cell showing the chemical composition  $\text{Li}_{7-x}\text{La}_3\text{M}_{2-x}\text{N}_x\text{O}_{12}$  ( $\text{M} = \text{Hf}, \text{Sn}, \text{Zr}$ ;  $\text{N} = \text{Na}, \text{Ta}$ ). In literature, lithium conductivities are reported, ranging from  $10^{-6} \text{ S}\cdot\text{cm}^{-1}$  up to  $10^{-3} \text{ S}\cdot\text{cm}^{-1}$  at 25 °C. One of the highest values was found in LLZO with cubic modification. Usually, undoped LLZO shows a tetragonal crystal structure at RT with reported bulk conductivities  $\sigma_{\text{bulk}}$  of  $10^{-6} \text{ S}\cdot\text{cm}^{-1}$  and an activation energy of 0.40-0.54 eV. [10],[11],[12]

For tetragonal modified LLZO with SG  $I4_1/acd$  (No. 142), the lattice constraints  $a = 1.3134(4) \text{ nm}$  and  $c = 1.2663(8) \text{ nm}$  were calculated. [12] A graphical representation is given in Fig. 1.1.

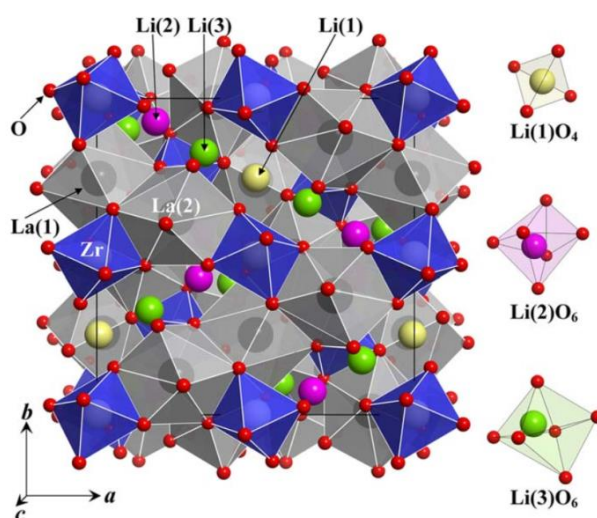


**Fig. 1.1: Schematic representation of tetragonal LLZO.  $\text{La}(1)\text{O}_8$  and  $\text{La}(2)\text{O}_8$  are dodecahedrons and  $\text{ZrO}_6$  represents a octahedron. Li sits on tetrahedral 8a and octahedral 16f and 32g, respectively. The reference is taken from [12].**

By doping the material by supervalent substitution at the Li, La or Zr site, it is possible to stabilize the cubic phase. Comparing the tetragonal and cubic phase, the cubic modification with SG  $Ia\bar{3}d$  (No. 230) and a lattice parameter of  $a = 1.29827(4) \text{ nm}$  in LLZO shows a lower activation energy, larger lattice constraints, higher densification and lower interactions of the Li-ion with other atoms in the crystal lattice. By supervalent substitution of cations like Al or

Ga on the Li site, the cubic structure can be stabilized showing the most promising results in ionic conductivity - one of the highest values could be found for cubic gallium doped LLZO resulting in  $\text{Li}_{6.4}\text{Ga}_{0.2}\text{La}_3\text{Zr}_2\text{O}_{12}$  with  $\sigma_{\text{total}} = 1.0 \cdot 10^{-3} \text{ S} \cdot \text{cm}^{-1}$  and  $E_a = 0.26 \text{ eV}$  at  $25 \text{ }^\circ\text{C}$ . As mentioned, this material has reportedly two stable phases – a cubic and a tetragonal phase depending on the supervalent substitution and stoichiometry. [13] Structural details of the cubic modification is given in Fig 1.2.

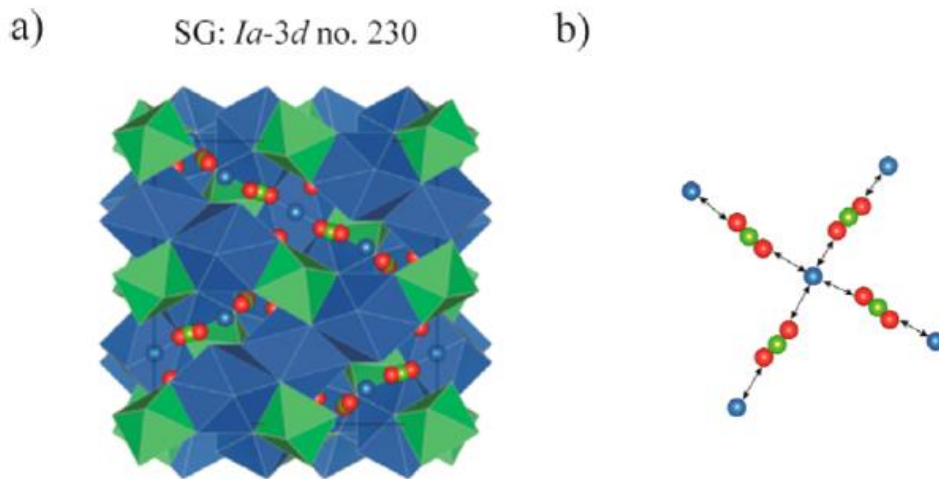


Fig. 1.2: Schematic representation of a) cubic LLZO with SG  $Ia\bar{3}d$  and b) corresponding diffusion pathway. Red spheres represent the tetrahedrally coordinated (24d) sites.  $\text{Zr}^{4+}$  occupies the 16a octahedra (green) and  $\text{La}^{3+}$  the 24c dodecahedra (blue). The figure is taken from reference [13].

Garnet-type materials with tetragonal and cubic crystal structures are well-established in literature and can be applied to many different ions. [14],[15],[16],[17] One of the most promising garnets is  $\text{Li}_7\text{La}_3\text{Zr}_2\text{O}_{12}$  because of its good results in stability and conductivity. [13],[18] As it shows promising results as a solid ionic conductor in the cubic phase, it is tried in this diploma thesis to synthesize stable phases of tetragonal LLHO and LLSO. Afterwards, both garnets are doped with  $\text{Ta}^{5+}$  on the  $\text{Hf}^{4+}$  and  $\text{Sn}^{4+}$  position in different stoichiometry up to completely exchanged positions to establish if stabilization of the cubic phase is possible as it was accomplished for LLZO. [6]

Furthermore, powder X-ray diffraction (PXRD) measurements are carried out to study how changing the composition of Hf, Sn and Ta influences the crystal structure due to different ionic radii of  $\text{Hf}^{4+}$ ,  $\text{Sn}^{4+}$  and  $\text{Ta}^{5+}$ . The ionic radii are given in Tab. 1.2.

Tab. 1.2: Ionic radii of Hf, Sn and Ta, taken from reference [19].

Element	Charge number	Coordination number	Ionic radius [pm]
Hf	4+	6	85
Sn	4+	6	83
Ta	5+	6	78

To determine to best composition of Ta doped LLHO and LLSO, respectively, by means of the ionic conductivity  $\sigma$  and activation energy  $E_a$ , electrochemical impedance spectroscopy (EIS) measurements are carried out.

## 2. General Aspects

In the following chapter, all important information and measuring techniques are described to help with the understanding of this diploma thesis.

### 2.1. Diffusion in Solids

Diffusion describes mass transport within a heterogeneous system including a concentration gradient. In this process inevitable defects are created in the crystal structure. Both mass transport and occurring defects in materials are described in the following subchapters. If not stated elsewhere, the following subchapters were cited from reference [20] and [21].

#### 2.1.1. Mass Transport

Diffusion processes in solids refer to mass transport through matter by atomic jumps within e.g. crystal lattices. This causes a change in the chemical composition in different regions of the material. Adolf Fick was the first to describe the movement of atoms in his first and second law of diffusion.

##### Fick's first law:

In order to describe the flux of diffusing particles, in e.g. molecules, atoms or ions, Fick's law has to be applied. If the flux in an isotropic medium happens in just one dimension, Fick's first law is written as

$$J = -D \cdot \frac{\Delta C}{\Delta x}, \quad (2.1)$$

where the diffusion flux of the particles is described by  $J$ , which is influenced by the opposite direction of the factor of proportionality  $D$ .  $D$  is also considered as the diffusion coefficient. The flux further depends on the change of the concentration  $\Delta C$  over a certain distance  $\Delta x$ . For real solids, Fick's law has to be adapted so that it can be used in three dimensions. Therefore, a vector notation for generalization of the one dimensional diffusion process has to be applied:

$$J = -D \cdot \nabla C \quad (2.2)$$

Here, the Nabbla symbol  $\nabla$  describes the vector operation on the right side of the equation. It produces the concentration gradient field  $\nabla C$  in x,y,z-direction. In isotropic media, the diffusion flux is antiparallel to the concentration gradient.

Equation of continuity:

If the number of particles stays constant over time, the equation of continuity (Eq. 2.3) can be applied. This condition is given, when the fluxes of entering and leaving particles in a certain volume and so the net accumulation (or loss) rate is balanced. The loss rate is expressed by

$$-\left[\frac{\partial J_x}{\partial x} + \frac{\partial J_y}{\partial y} + \frac{\partial J_z}{\partial z}\right] \Delta x \Delta y \Delta z = \frac{\partial C}{\partial t} \Delta x \Delta y \Delta z, \quad (2.3)$$

which describes the particle flux in x,y,z-direction in terms of the time derivative of the concentration. Eq. 2.3 can then be simplified, which gives the equation of continuity

$$-\nabla \cdot J = \frac{\partial C}{\partial t} \quad (2.4)$$

by introducing the vector operation divergence  $\nabla$ .

**Fick's second law:**

By combining Fick's first law (Eq. 2.2) with the equation of continuity (Eq.2.4), Fick's second law, or diffusion equation, can be introduced by

$$\frac{\partial C}{\partial t} = \nabla \cdot (D \nabla C). \quad (2.5)$$

Eq. 2.5 is a second-order partial differential equation and describes the depletion of the concentration, which is proportional to  $D$ . Fick's second law is not linear, if diffusion occurs in a chemical composition gradient. If  $D$  depends on the composition it is often called interdiffusion coefficient. If it does not depend on the concentration, which is the case in chemically homogeneous systems, Eq. 2.5 can be simplified to the second-order partial differential equation

$$\frac{\partial C}{\partial t} = D \Delta C. \quad (2.6)$$

It is also denoted the linear diffusion equation, where  $\Delta$  describes the Laplace operator for the direction and time dependent concentration field  $C(x,y,z,t)$ . Eq. 2.6 can be solved if initial and boundary conditions are set first.

### 2.1.2. Inter-atomic Diffusion Processes

By looking at a crystal lattice, each atom has a preferred position with a certain energetically lowest ground state. To make mass transport possible, thermal energy has to be applied to the system making it possible to overcome the energy level of the atoms. This energy level is also denoted as barrier energy that is needed to break inter-atomic bonds by vibrational energy. It allows the migration from one lattice site to another one if the adjacent site is empty.

In this case, two types of diffusion mechanisms are possible:

#### 1. vacancy diffusion

The diffusing atom uses vacancies within the crystal lattice for changing the position (Fig. 2.1).

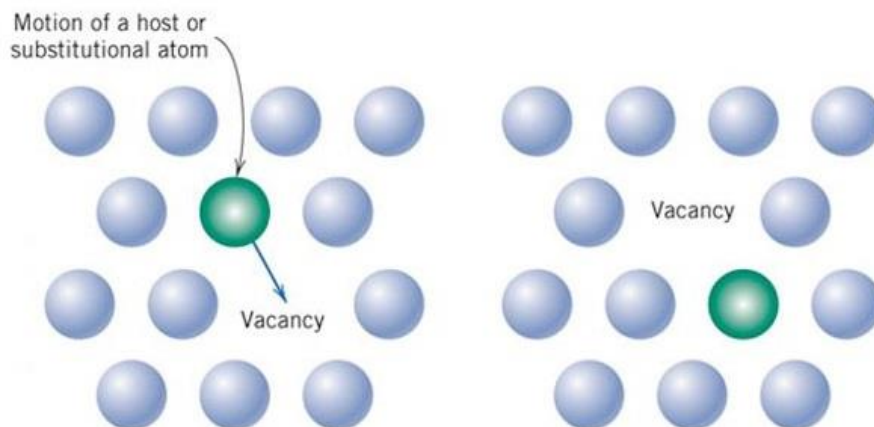


Fig. 2.1: Mechanism of the vacancy diffusion. The blue points represent the matrix of the crystal lattice, the green circle the jumping particle before (left) and after (right) migration. The figure is taken from reference [22].

#### 2. interstitial diffusion

The atom jumps on the empty interstitial positions of the crystal lattice without causing a displacement of vacancies or other atoms (Fig. 2.2).

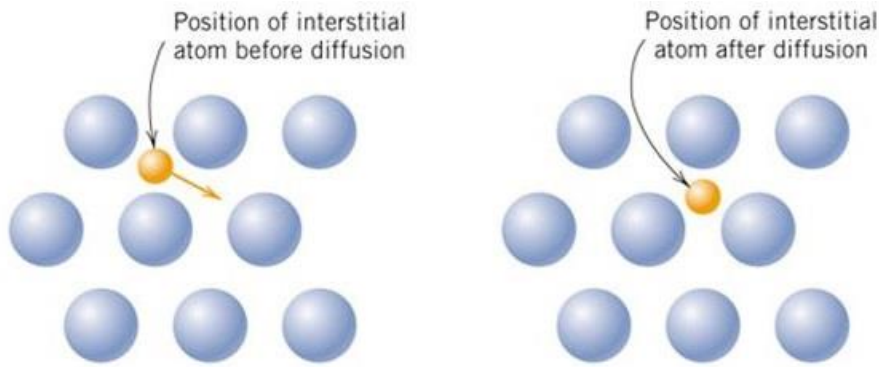


Fig. 2.2: Mechanism of the interstitial diffusion. The blue points represent the matrix of the crystal lattice, the orange circle the jumping particle before (left) and after (right) migration. The figure is taken from reference [22].

In both jump processes from one position to another, the particle has to pass neighboring atoms in the crystal lattice, which, especially in interstitial diffusion, causes a compression and deformation of the jumping atom, respectively. This process requires a lot of energy with respect to the thermal energy  $k_B T$ .

In crystal lattices at finite temperatures atoms oscillate around their equilibrium point. This oscillation is usually not strong enough to overcome the barrier energy for diffusion, which causes the particle to fall back to its initial energy level or ground state. Only if the saddle point barrier energy (or activation energy)  $E_m$  (Fig. 2.3) is supplied, the atom is able to pass the energetic unfavorable point by breaking the inter-atomic bonds through vibrational energy.

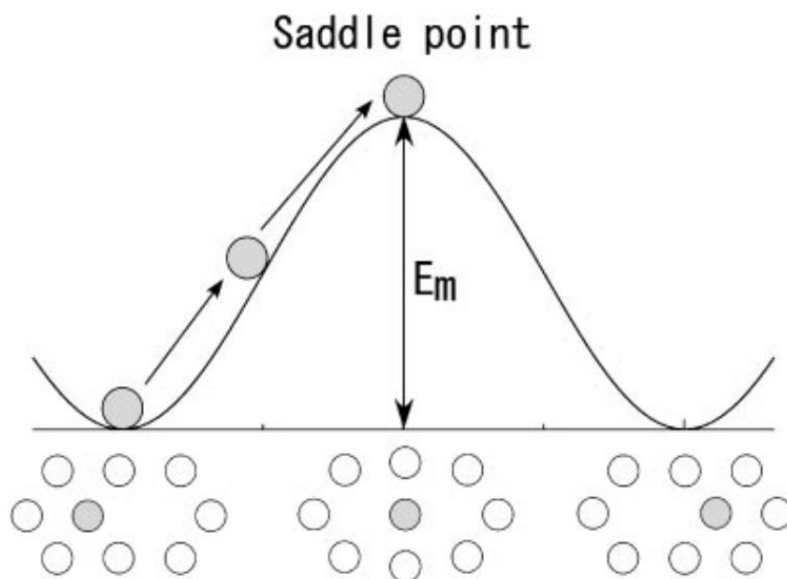


Fig. 2.3: Schematic representation of vacancy migration. The white points represent the matrix of the crystal lattice; the grey circle is the jumping particle.  $E_m$  shows the energy difference between the activated and ground state. The figure is taken from reference [3].

$E_m$  is also called *Gibb's free enthalpy of migration*  $G_m$ . It is described as the energy difference between the ground state and the saddle point energy and will be further described in chapter 2.1.3. The jump rate of the vacancies  $\Gamma$  is given by

$$\Gamma = \Gamma_0 \cdot \exp\left(-\frac{E_A}{k_B T}\right), \quad (2.7)$$

where  $\Gamma_0$  denotes the premultiplying factor. The activation energy of the jump processes is represented by  $E_A$ ,  $k_B$  denotes the Boltzmann constant and  $T$  the temperature. [23]

### 2.1.3. Defects

Theoretically, it is possible to obtain a perfect crystal without any defects and a perfect crystal lattice at 0 K because atomic movement completely stops due to lacking thermal energy. At temperatures above 0 K, a crystal always shows a certain imperfection and defects in the lattice, which is caused by oscillating particles. This effect is initiated by a reduction of the free energy  $\Delta G$ , which is influenced by the entropy  $\Delta S$  that is caused and the amount of energy  $\Delta H$  that is needed to create a vacancy. The relation between  $\Delta G$ ,  $\Delta H$  and  $\Delta S$  at a certain temperature  $T$  is given by

$$\Delta G = \Delta H - T \cdot \Delta S. \quad (2.8)$$

In contrast to ideal crystals defects are present in classical solid ion conductors and the conductivity depends on the movability of both self-interstitials and vacancies in the lattice. Defects, in general, can be separated into stoichiometric and non-stoichiometric defects. In stoichiometric defects, the composition of the crystal stays unchanged while defects are introduced. In non-stoichiometric defects, the composition changes for implementing defects in the lattice. Additionally, a classification in three groups regarding the shape and size of the defects was made. These classes are:

1. Point defects: They describe defects involving one atom or site that may infect neighboring atoms. Vacancies and interstitials are formed only one-dimensionally.
2. Line defects or dislocations: Defects that occur two-dimensionally. Line defects are distinguished in edge and screw dislocations depending on the region where dislocation occurs.
3. Plane defects: They are three-dimensional and include defects in all layers of a crystal structure.

In this diploma thesis, only point defects are from interest, which is why they are further described.

## Point defects

These one-dimensional defects include mixed crystals, impurities and Schottky and Frenkel disorder.

1. Mixed crystals: The statistical distribution of the components itself create defects. The formation of a mixed crystal formed by different ions creates point defects.
2. Impurities: In an ideal crystal, the purity should be given by 100 % which sums up to  $10^{23}$  atoms in  $1 \text{ cm}^3$ . Even if only 0.00001 % of the crystal contains impurities, this would sum up to  $10^{16}$  impurity atoms. These are usually bigger or smaller than the predominant atoms in the crystal structure. Bonds with foreign atoms can further lead to increasing point defects.
3. Frenkel-Schottky-disorder: Vacancies can be found in every crystal structure. In Frenkel defects (Fig. 2.4c), cations leave their regular lattice site and jump to an interstitial site, which is normally not filled. This effect can be found, e.g. in AgCl, where  $\text{Ag}^+$  acts as the interstitial atom. Due to possible covalent interactions of an interstitial atom with surrounding  $\text{Ag}^+$  and  $\text{Cl}^-$  ions, the defect gets stabilized by neighboring atoms. In Schottky defects (Fig. 2.4a), both cations and anions leave their lattice site and move to the surface of the crystal creating two vacancies. To preserve electroneutrality, the same amount of cations and anions is involved in this process.

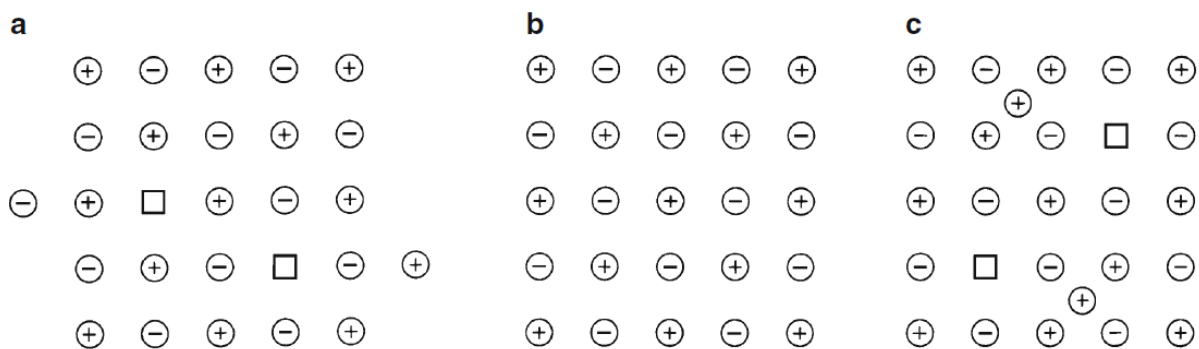


Fig. 2.4: Representation of Schottky- (a) and Frenkel (c) defect in comparison to an ideal crystal lattice (b). Circles with a '+' represent cations, circles with '-' show anions. Vacancies are represented by squares. The figure was taken from reference [21].

## 2.2. X-Ray Diffraction

X-rays are electromagnetic radiations with wavelengths between 0.05 to 0.23 nm. They are used for the determination and characterization of powders as a very common and well-known method for solid materials to gain information about the crystal structure on an atomic scale. With this technique it is further possible to get information about the unit cell

parameters and to determine the position of the atoms in orders of  $10^{-4}$  nm. Additionally, it is possible to determine the crystallinity and identify the phases of different materials. [24]

In principle, diffraction can be observed when electromagnetic radiation interacts with the three-dimensional periodic structure of solids. This structure is a framework made of atoms with mean distances of 0.15-0.40 nm to adjacent particles. The distance corresponds with the wavelengths of X-rays. Due to the fact that both the lattice constraint and the wavelength of the X-ray radiation are in the same dimension, diffraction is possible. [10]

For later understanding, the Miller indices ( $hkl$ ) and their relation to interplanar distances  $d$  are briefly explained.

### 2.2.1. Miller Indices

Because diffractions of real crystals are hard to visualize, crystallographic planes were introduced. These are also called Miller or crystallographic indices and are described by the three integer indices,  $h$ ,  $k$  and  $l$ . They define the reciprocal space in all three dimensions, which represents the Fourier transformed Bravais lattice. Nonetheless, these indices are only used as a concept and are not present in real crystals. Miller indices are defined as a set of planes, which intersect all lattice planes. They are equally spaced and oriented parallel to each other with a certain distance to adjacent planes. This distance is also called d-spacing. [25]

### 2.2.2. Laue Equation

For defining symmetry elements with the preferred direction of a crystal, crystallographic point groups were established, which sum up to a total number of 32. [21]

In diffraction of X-rays, incident electromagnetic radiation interacts with the crystal so that the outgoing waves always result in a centrosymmetric pattern. Even if an inversion center is existent, this effect is not influenced. To describe and characterize the geometry of X-ray diffraction on a crystal lattice, the Laue classes were set up. They give the relation between incoming and diffracted waves in every direction of the unit cell, which gives the Laue equations:

$$\begin{aligned}a (\cos \Psi_1 - \sin \varphi_1) &= h \lambda \\b (\cos \Psi_2 - \sin \varphi_2) &= k \lambda \\c (\cos \Psi_3 - \sin \varphi_3) &= l \lambda\end{aligned}\tag{2.9}$$

The dimensions of the unit cell are given by  $a$ ,  $b$  and  $c$ .  $\Psi_i$  and  $\varphi_i$  and their direction cosines,  $\cos \Psi_i$  and  $\cos \varphi_i$ , denote angles of the incoming and outgoing waves.  $\lambda$  is the radiation wavelength.  $h$ ,  $k$  and  $l$  are called the Miller indices and have the same meaning as in chapter 2.2.1. Only if all three equations are satisfied, diffraction reflections can be observed.

This is given, because the lattice distances in the unit cell  $a$ ,  $b$  and  $c$  and the wavelength  $\lambda$  have diffraction maxima at certain angles in repeating unit cells. These relations were later simplified by William Lawrence Bragg, who introduced the correspondent equation, which is the basis for PXRD measurements. [25]

### 2.2.3. Bragg Equation

The diffraction of X-rays is based on constructive interferences between a crystalline sample and the monochromatic X-rays. This radiation was firstly generated by a cathode ray tube, filtered and collimated so that only X-rays with a certain wavelength  $\lambda$  interact with the sample. When electromagnetic radiation impinges on crystal structures it is reflected at the lattice planes. These are oriented parallel to each other and always have the same interplanar distance  $d$  to adjacent planes. Constructive interference can then only occur, if the detected angle of the scattered X-rays is equal to angle  $\theta$  of the incident beam. The relation between the incoming monochromatic wavelength  $\lambda$ , the interplanar spacing  $d$  and the diffraction angle  $\theta$  is described by the Bragg's law or Bragg condition (Eq. 2.10).

Only if

$$n \cdot \lambda = 2 \cdot d \cdot \sin(\theta) \quad (2.10)$$

is satisfied, a diffraction beam can be detected. In Eq. 2.10,  $n \in \mathbb{N}$  is called the order of reflection and describes the integer multiple of the wavelength of adjacent reflected beams. [25] A graphical illustration is given in Fig. 2.5.

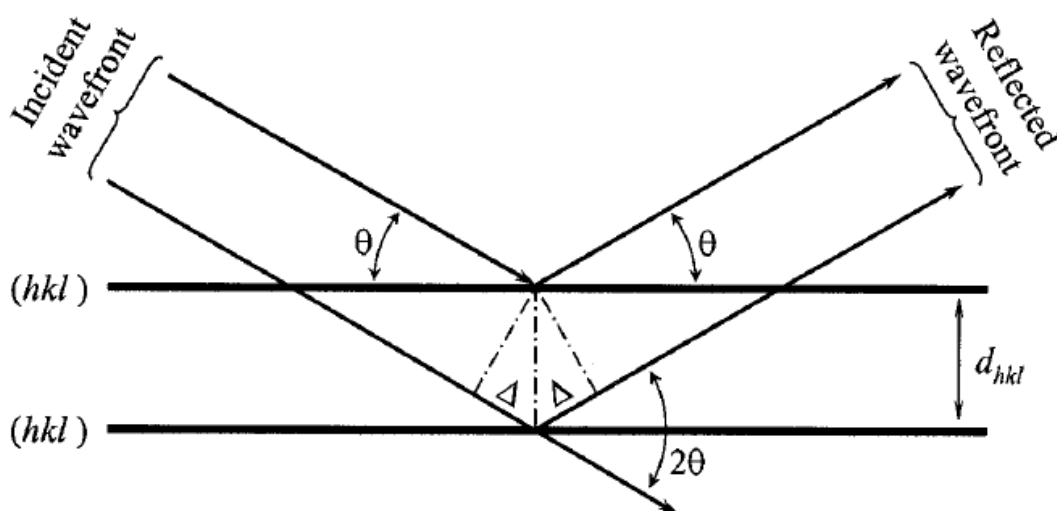


Fig. 2.5: Graphical representation of Bragg's law.  $\theta$  denotes the angle of the incident and diffracted X-ray beam,  $d_{hkl}$  is the distance between the lattice planes  $(hkl)$ . The figure is taken from reference [25].

## 2.3. Impedance Spectroscopy

### 2.3.1. Impedance

Impedance Spectroscopy is a technique that is used for many different purposes ranging from measuring the interfacial behavior of molecules to testing the functionality of batteries by measuring the alternating current (AC) resistance. In lithium metal oxides, which were prepared in this diploma thesis, the ionic conductivity results from ion hopping. [26]

To resist the electrical current flow, a circuit element has an electrical resistance, which is described by Ohm's law (Eq. 2.11).

$$R = \frac{E}{I} \quad (2.11)$$

Here,  $R$  denotes the resistance,  $E$  the voltage and  $I$  the current. Ohm's law is, however, an ideal resistor, which is why it is limited to one circuit element. This means that the resistance is independent of the frequency and the voltage and AC current are always in phase following Ohm's law at all levels. For the determination of the ongoing processes capacitance and resistance is needed. Therefore, an RC element needs to be introduced:

$$\tau = R \cdot C \quad (2.12)$$

with

$$R \cdot C = \frac{1}{\omega} \quad (2.13)$$

Here,  $\tau$  denotes the time constant and  $\omega$  represents the radial frequency. The relation between the radial frequency  $\omega$  and the alternating frequency  $\nu$  is given by

$$\omega = \nu \cdot 2 \cdot \pi. \quad (2.14)$$

In reality, more than one circuit element can be found, not showing ideal properties. This makes it inevitable to introduce impedance because real resistors always involve capacitance, inductance, resistance and a time delay of response, respectively. Over wide frequency ranges, the resistor can be approximated in equivalent circuits by ideal resistance. Over all frequencies, the equivalent circuit exhibits the resistance, which then gives an immediate instead of a delayed response to the electric stimulus.

Impedance functions like resistance, but is not limited to the simplification. In EIS a sinusoidal AC potential is applied for measuring the steady-state current flow  $I(t)$  in the cell by

$$V(t) = V_0 \cdot \sin(\omega t). \quad (2.15)$$

Here,  $V(t)$  is the potential at time  $t$ ,  $V_0$  is the amplitude with a radial frequency  $\omega$ . The response is pseudo-linear. This means that a sinusoidal potential with the same frequency is measured, but the resulting current

$$I(t) = I_0 \cdot \sin(\omega t + \phi) \quad (2.16)$$

is shifted in phase by  $\phi$  (Fig. 2.6). [27],[28]

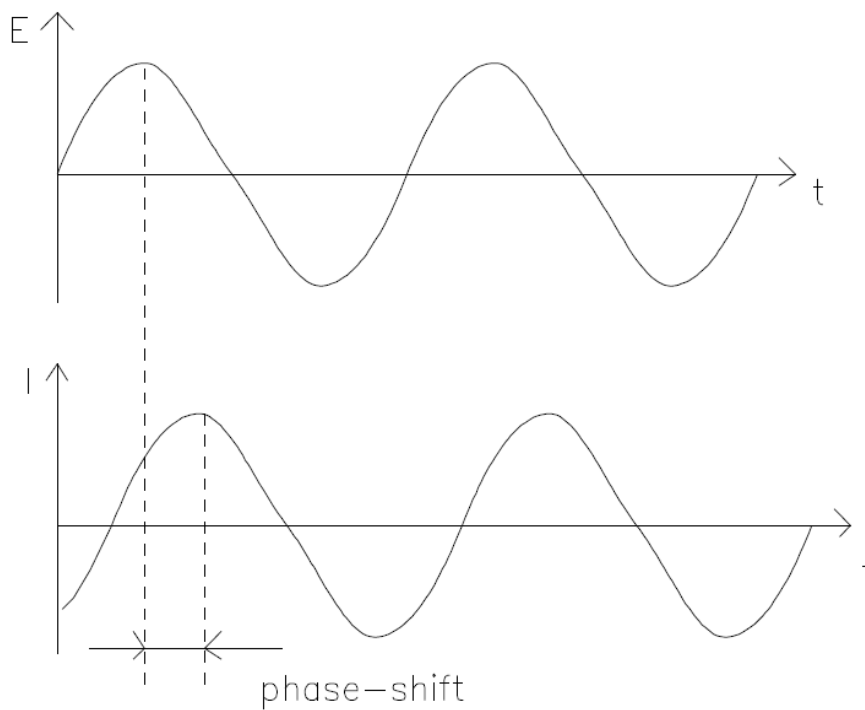


**Fig. 2.6: Sinusoidal current response in a (pseudo)-linear system. The figure is taken from reference [28].**

The impedance  $Z$  can then be expressed analogously to the ohmic law (Eq. 2.11) and gives the resistance by

$$Z = \frac{V(t)}{I(t)} = \frac{V_0 \cdot \sin(\omega t)}{I_0 \cdot \sin(\omega t + \phi)} = Z_0 \frac{\sin(\omega t)}{\sin(\omega t + \phi)}. \quad (2.17)$$

The impedance can also be expressed as a complex function by introducing the Euler relationship

$$e^{i\phi} = \cos \phi + i \sin \phi \quad (2.18)$$

with  $i = \sqrt{-1}$ . Taking Eq. 2.17 into account, it results in the complex impedance

$$Z(\omega) = Z_0 e^{i\phi} = Z_0 (\cos \phi + i \sin \phi) \quad (2.19)$$

with the complex potential

$$V_i(t) = V_0 \cdot e^{i\omega t} \quad (2.20)$$

and the complex current

$$I_i(t) = I_0 \cdot e^{i\omega t + \phi}. \quad (2.21)$$

In conventional EIS, the impedance is measured in dependence of  $\omega$  and the temperature. Eq. 2.19 can then be separated into a real and imaginary part of the impedance, denoted as  $Z'$  and  $Z''$ :

$$Z(\omega) = Z' + i \cdot Z''. \quad (2.22)$$

With  $Z'$  and  $Z''$ , it is then possible to determine resistances within the material, displayed in the Nyquist plot. [27] An explanation of the Nyquist plot is given in chapter 2.3.3.

### 2.3.2. Conductivity Isotherms

Conductivity isotherms are used as a common way in impedance spectroscopy to determine the direct current (DC) conductivity, to separate different electrochemical processes in materials and to, furthermore, calculate the activation energy of the sample. These isotherms can be observed if the real part of the conductivity  $\sigma'$  is plotted vs. the frequency  $\nu$ . A double-logarithmic scale is chosen for the conductivity spectrum. [29] A graphical representation of a typical isotherm can be seen in Fig. 2.7.

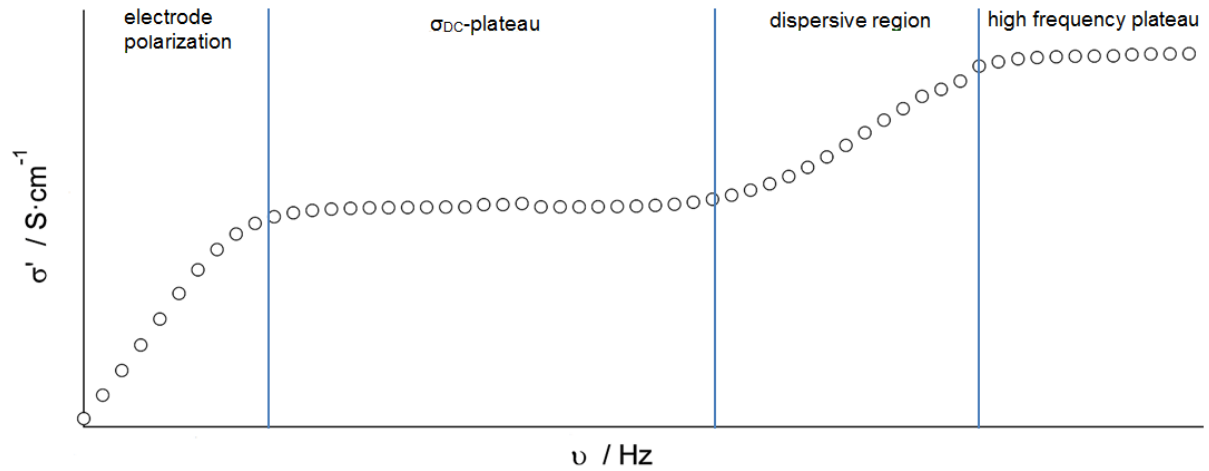


Fig. 2.7: Graphical representation of a typical conductivity isotherm. The blue lines give an optical separation of the curve in four regions.

In Fig. 2.7, four characteristic regions of conductivity isotherms, separated by three blue lines, can be seen. The first one describes electrode polarization (EB), predominant at low frequencies and high temperatures. This is connected to high mobility of ions accumulating to the surface of the Au electrodes, which were firstly applied on the sample. When moving to higher frequencies, a frequency independent plateau, the conductivity isotherm, can be observed. At this plateau, processes like grain boundary or bulk processes within the sample can be detected. It is also called  $\sigma_{DC}$ -plateau, if long-rang ion transport and thus bulk processes can be identified. It is then further possible to determine the thermal activation energy due to a linear correlation of the conductivity vs. the temperature. Plotting  $\log(\sigma_{DC} \cdot T)$  vs.  $1000 \cdot T^{-1}$  results into the Arrhenius plot. The activation energy can then be calculated as  $\sigma_{DC} \cdot T$  follows Arrhenius behavior, given by

$$\sigma_{DC} = \sigma_0 \cdot \exp\left(-\frac{E_A}{k_B T}\right). \quad (2.23)$$

Here,  $\sigma_0$  represents the pre-exponential factor.  $E_A$  and  $k_B$  denote the activation energy and the Boltzmann constant, respectively. [30],[31]

This isotherm is followed by a dispersive region with increasing frequency. At this region, the conductivity again experiences a weak dependency on the frequency followed by a second plateau at high frequencies. [29]

### 2.3.3. Nyquist Plot

The Nyquist (or Cole-Cole) plots are used for a better understanding of electric properties within different solid electrolytes regarding the impedance and the bulk and grain boundary conductivity, respectively. These properties are described by the combination of capacitance

and resistance elements, which are called equivalent circuits. If not stated elsewhere, the following subchapter was cited from reference [32].

In an equivalent circuit, it is possible to arrange the capacitor and ohmic resistor either parallel or in series. This gives the impedance of the capacitance  $Z_C$  (Eq. 2.24) and the resistance  $Z_R$  (Eq. 2.25):

$$Z_C = -i \cdot \frac{1}{\omega C} \quad (2.24)$$

$$Z_R = R, \quad (2.25)$$

where  $C$  denotes the capacitance,  $\omega$  is the frequency and  $R$  represents the resistance. By reciprocal combination of  $Z_C$  and  $Z_R$ , the impedance of the equivalent circuit is observed, resulting in a linear behavior

$$Z_{el} = R_{el}. \quad (2.26)$$

Eq. 2.26 is then used to calculate the real part  $Z'$  (Eq. 2.27) and the imaginary part  $Z''$  (Eq. 2.28) of the impedance for serial and parallel connection, respectively, by

$$Z' = R_{el} + \frac{R_{ct}}{\omega^2 R_{ct}^2 C_{dl}^2} \quad (2.27)$$

$$-Z'' = \frac{\omega R_{ct}^2 C_{dl}}{1 + \omega^2 R_{ct}^2 C_{dl}^2}. \quad (2.28)$$

Here,  $R_{el}$  and  $R_{ct}$  denote an ideally polarizable electrode and a charge transfer electrode, respectively, and  $C_{dl}$  represents the capacitance of the electrode.

By plotting the negative imaginary part  $-Z''$  vs. the real part  $Z'$  of the impedance, the Nyquist plot is observed.

If the electrode is ideally polarizable and  $C$  and  $R$  are connected in series (Fig. 2.8a), the equivalent circuit shows a linear behavior between the ohmic resistance and the double layer capacitance, seen in Fig. 2.8b.

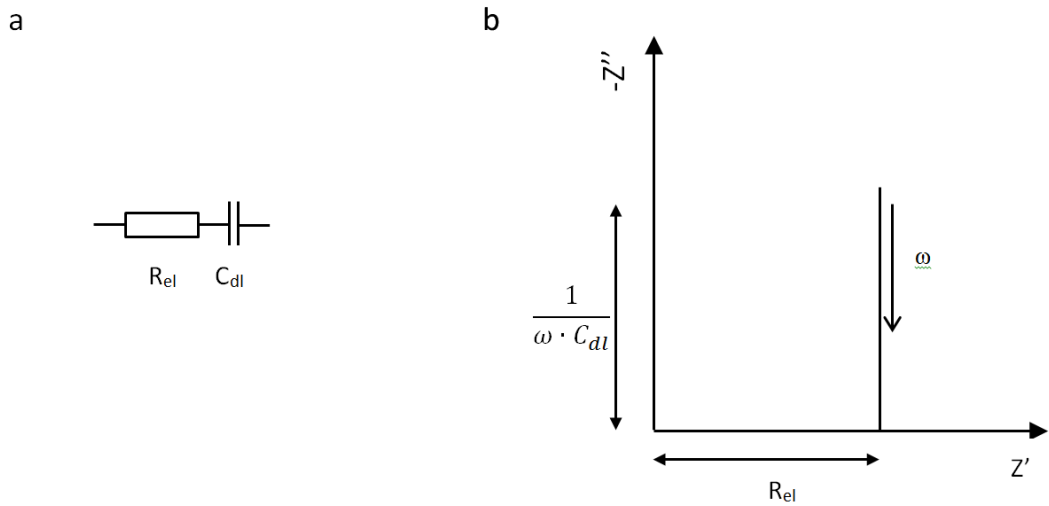


Fig. 2.8: a) Equivalent circuit with electrolyte resistance  $R_{el}$  and capacitance  $C_{dl}$  in series. b) Schematic representation of a Nyquist plot for  $-Z''$  vs.  $Z'$  as a function of the frequency  $\omega$  in serial connection.

Fig. 2.9 shows a capacitor and resistor in parallel connection (a). The resulting Nyquist plot (b) gives the characteristic semicircle of the complex impedance.

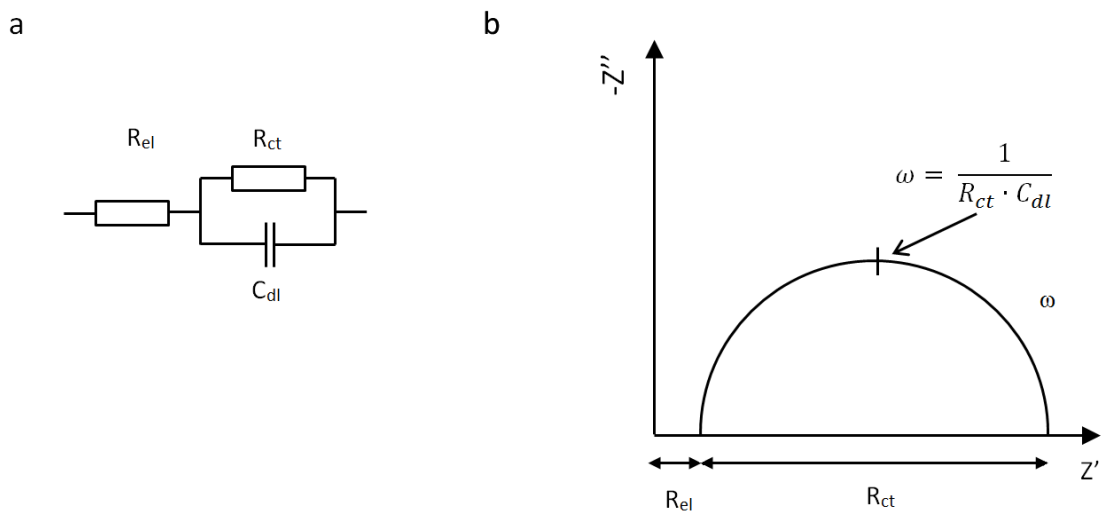


Fig. 2.9: a) Equivalent circuit with  $R_{el}$ ,  $R_{ct}$  and  $C_{dl}$  in parallel connection. b) Schematic representation of a Nyquist plot for  $-Z''$  vs.  $Z'$  as a function of the frequency  $\omega$  in parallel connection.

# 3. Experimental

In the following chapters, the syntheses and used measurement methods for characterization of  $\text{Li}_{7-x}\text{La}_3\text{Hf}_{2-x}\text{Ta}_x\text{O}_{12}$  and  $\text{Li}_{7-x}\text{La}_3\text{Sn}_{2-x}\text{Ta}_x\text{O}_{12}$  are described.

All chemicals were purchased from commercial suppliers and not further purified.

## 3.1. $\text{Li}_{7-x}\text{La}_3\text{Hf}_{2-x}\text{Ta}_x\text{O}_{12}$ (Ta-LLHO)

Polycrystalline  $\text{Li}_{7-x}\text{La}_3\text{Hf}_{2-x}\text{Ta}_x\text{O}_{12}$  with different ratios of Hf and Ta were prepared by the following reaction:



For obtaining single-phase garnets of  $\text{Li}_{7-x}\text{La}_3\text{Hf}_{2-x}\text{Ta}_x\text{O}_{12}$  with different amounts of Ta, the syntheses were prepared by a standard solid state reaction. This method, in general, was separated into three steps:

- Mixing
- Calcination
- Sintering

### **Mixing**

Stoichiometric amounts of  $\text{Li}_2\text{CO}_3$  (>99 %, Sigma-Aldrich),  $\text{La}_2\text{O}_3$  (>99.5 %, Merck),  $\text{HfO}_2$  (99 %, MaTeck) and  $\text{Ta}_2\text{O}_5$  (99 %, Sigma-Aldrich) were prepared. Due to lithium loss during the high temperature heat treatment in the sintering process, a molar excess of 10 % of  $\text{Li}_2\text{CO}_3$  was added. [33]

Afterwards, the powder was put into a mortar. Some milliliters of isopropanol were added in order to obtain a homogeneous slurry while pestling. When most of the isopropanol has evaporated the powder was put into a heating oven overnight in order to remove the remaining isopropanol. The compositions can be seen in Tab. 3.1.

Tab. 3.1: Composition of the Ta doped LLHO.

Sample description	Composition
0.00 Ta-LLHO	$\text{Li}_7\text{La}_3\text{Hf}_2\text{O}_{12}$
0.25 Ta-LLHO	$\text{Li}_{6.75}\text{La}_3\text{Hf}_{1.75}\text{Ta}_{0.25}\text{O}_{12}$
0.50 Ta-LLHO	$\text{Li}_{6.5}\text{La}_3\text{Hf}_{1.5}\text{Ta}_{0.5}\text{O}_{12}$
0.75 Ta-LLHO	$\text{Li}_{6.25}\text{La}_3\text{Hf}_{1.25}\text{Ta}_{0.75}\text{O}_{12}$
1.00 Ta-LLHO	$\text{Li}_6\text{La}_3\text{HfTaO}_{12}$
1.25 Ta-LLHO	$\text{Li}_{5.75}\text{La}_3\text{Hf}_{0.75}\text{Ta}_{1.25}\text{O}_{12}$
1.50 Ta-LLHO	$\text{Li}_{5.5}\text{La}_3\text{Hf}_{0.5}\text{Ta}_{1.50}\text{O}_{12}$
1.75 Ta-LLHO	$\text{Li}_{5.25}\text{La}_3\text{Hf}_{0.25}\text{Ta}_{1.75}\text{O}_{12}$
2.00 Ta-LLHO	$\text{Li}_5\text{La}_3\text{Ta}_2\text{O}_{12}$

For the sake of simplicity, the sample descriptions are further used.

### Calcination

For the calcination step, the dry powder was pressed into pellets with a diameter of 13 mm. Therefore, uniaxial pressure of approximately 5-10 kN for about 30 to 60 seconds (s) was applied. Afterwards the samples were put into a ceramic crucible. To reduce contamination, the following setup was chosen (Fig. 3.1):

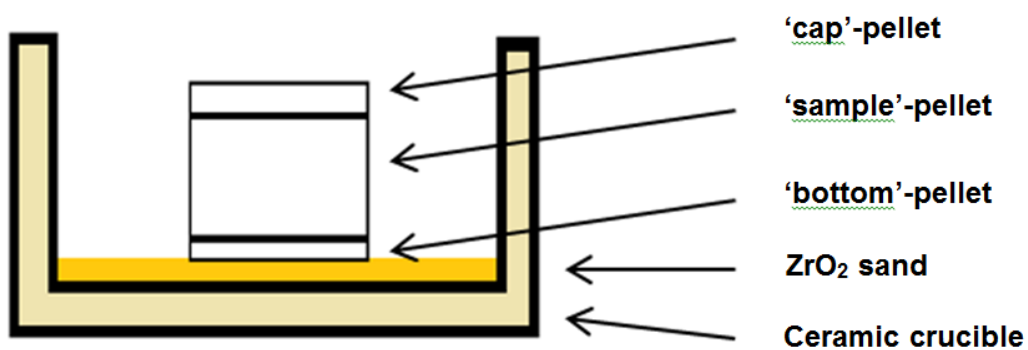


Fig. 3.1: Setup for calcination.

The bottom of the crucible was covered with ZrO<sub>2</sub> sand to reduce possible contamination with aluminum. [34] On this, a 'bottom-pellet' with a height of approximately 1 mm, which was made of the original material, was put onto the powder. On this 'bottom-pellet' the pressed

samples, which should further be sintered, were placed. They were then covered by a 'cap-pellet' to decrease lithium loss during the calcination process. [33] After arranging the setup, the samples were put into a Carbolite CWF 1300 oven.

#### Heating program for the calcination

The following heat treatment was used for the whole Ta-LLHO series (Fig. 3.2):

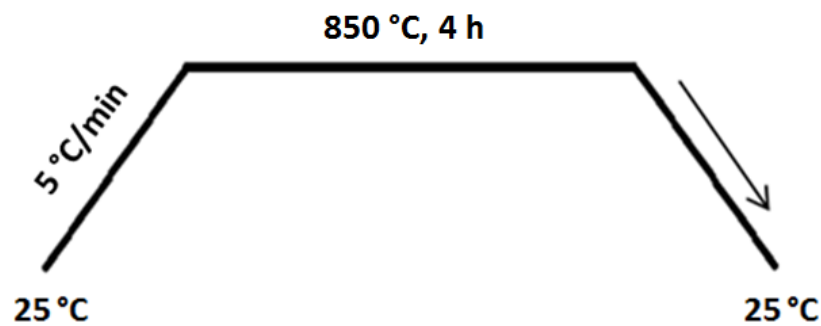


Fig. 3.2: Temperature program of the calcination process.

The pellets were firstly heated up from RT to 850 °C with a heating rate of 5 °C/minute (min). This temperature was held for 4 hours (h). The heating program was then stopped and the samples were left to stand for natural cooling to RT.

Afterwards, the pellets were separated from the 'bottom'- and 'cap'-pellets. Some of them were then reground in a mortar for approximately 5 min until a finely granulated powder was obtained. Some other pellets were ball milled in a Fritsch Pulverisette 7 Premium line planetary ball mill in a 45 mL beaker, which got filled with 3 g of each reactant and 180 ZrO<sub>2</sub> milling balls with a diameter of 5 mm before being granulated. A rotational speed of 500 rounds per minute (rpm) was used for a total of 2 h. This time consisted of 12 cycles, which were divided into 5 min of milling and 5 min of resting to avoid overheating. Both the reground and milled granulates were further used in the sintering step.

#### Sintering

For this step, the granulate was pressed again with uniaxial pressure of 5-10 kN for 30-60 s, whereas different dimensions for the 'bottom'- and 'cap'-pellets and the sample pellets itself were chosen. The dimensions of the pellets are given in Tab.3.2.

Tab. 3.2: General pellet dimensions.

pellet	Diameter [mm]	Approximated height [mm]
bottom	13	0.5-1.5
cap	13	0.5-1.5
sample	10	1.0-1.5

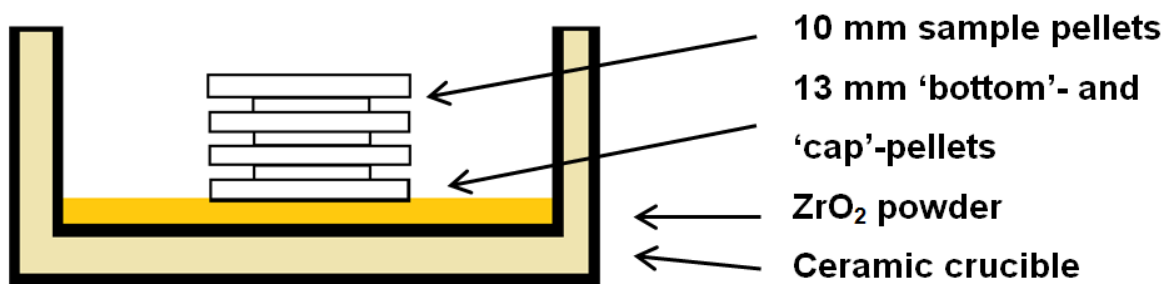


Fig. 3.3: Setup for the sintering process.

For each heat treatment, the samples were arranged as seen in Fig. 3.3. Afterwards, the samples were treated at different temperatures, whereas a heating speed of 5 °C/min and natural cooling to RT were chosen in all processes. The general program of the sintering process can be seen in Fig. 3.4. Used temperatures and holding times can be taken from Tab. 4.1 in chapter 4.1.2.

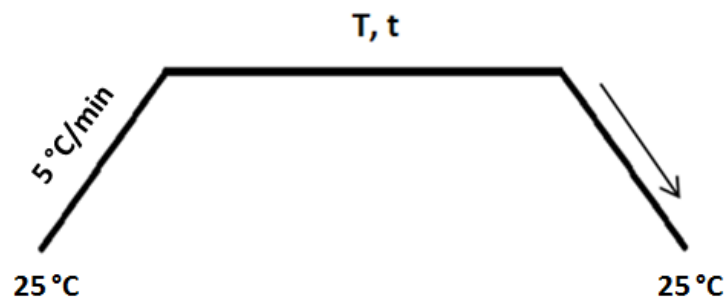


Fig. 3.4: General temperature program of the sintering process.

## 3.2. $\text{Li}_{7-x}\text{La}_3\text{Sn}_{2-x}\text{Ta}_x\text{O}_{12}$ (Ta-LLSO)

Polycrystalline  $\text{Li}_{7-x}\text{La}_3\text{Hf}_{2-x}\text{Ta}_x\text{O}_{12}$  were prepared according to the following reaction:



For the syntheses, stoichiometric amounts of  $\text{Li}_2\text{CO}_3$  (>99 %, Sigma-Aldrich),  $\text{La}_2\text{O}_3$  (>99.5 %, Merck),  $\text{SnO}_2$  (99.9 %, Sigma-Aldrich) and  $\text{Ta}_2\text{O}_5$  (99 %, Sigma-Aldrich) were prepared. A molar excess of 10 % of  $\text{Li}_2\text{CO}_3$  was again added due to Li loss during the high temperature heat treatment in the sintering process. [35] Milling and calcination was carried out in the same way as for undoped and doped Ta-LLHO, seen in chapter 3.1. The compositions of the mixtures are given in Tab. 3.3:

**Tab. 3.3: Composition of the Ta doped LLSO.**

Sample description	Composition
0.00 Ta-LLSO	$\text{Li}_7\text{La}_3\text{Sn}_2\text{O}_{12}$
0.25 Ta-LLSO	$\text{Li}_{6.75}\text{La}_3\text{Sn}_{1.75}\text{Ta}_{0.25}\text{O}_{12}$
0.50 Ta-LLSO	$\text{Li}_{6.5}\text{La}_3\text{Sn}_{1.5}\text{Ta}_{0.5}\text{O}_{12}$
0.75 Ta-LLSO	$\text{Li}_{6.25}\text{La}_3\text{Sn}_{1.25}\text{Ta}_{0.75}\text{O}_{12}$
1.00 Ta-LLSO	$\text{Li}_6\text{La}_3\text{SnTaO}_{12}$
1.25 Ta-LLSO	$\text{Li}_{5.75}\text{La}_3\text{Sn}_{0.75}\text{Ta}_{1.25}\text{O}_{12}$
1.50 Ta-LLSO	$\text{Li}_{5.5}\text{La}_3\text{Sn}_{0.5}\text{Ta}_{1.50}\text{O}_{12}$
1.75 Ta-LLSO	$\text{Li}_{5.25}\text{La}_3\text{Sn}_{0.25}\text{Ta}_{1.75}\text{O}_{12}$
2.00 Ta-LLSO	$\text{Li}_5\text{La}_3\text{Ta}_2\text{O}_{12}$

Analogue to Ta-LLHO, the sample descriptions are further used for simplicity.

For the sintering process, the same setup (Fig. 3.3) and heating program (Fig. 3.4) were chosen. The heat treatment used for Ta-LLSO can be seen in Tab. 4.7 in chapter 4.2.2.

### 3.3. Characterization

For determination of the total amount of reactant losses during the heating process, differential thermal analysis coupled with thermogravimetry (DTA-TG) measurements were carried out for the calcinated samples of LLHO and LLSO in a temperature range between 25 °C and 1400 °C in open ceramic crucibles with a heating and cooling rate of 10 °C/min under 40 ml/min N<sub>2</sub>, 40 ml/min protective N<sub>2</sub> and 20 ml/min O<sub>2</sub> flow using a Netzsch STA 449 F1 coupled with a Netzsch QMS 403 C.

PXRD measurements were performed on powders from reground samples to establish phase purity, the crystal structure and lattice parameter, respectively, using a Bruker D8 Advance diffractometer with Bragg Brentano geometry and Cu-K $\alpha$ -radiation ( $\lambda=1.5406$  Å) in the range  $10^\circ \leq 2\theta \leq 60^\circ$ . PXRD measurements were recorded right after the synthesis. Unit cell parameters were determined by Rietveld refinement using the program X'Pert HighScore Plus.

EIS measurements were carried out using the sintered pellets with thicknesses of approximately 1-2.5 mm and diameters of about 8-10 mm, which were first abraded on the surface with a Hermes P 800 abrasive paper. As the electrode material pellets were coated with 100 nm of Au by evaporation at 40 mA in a Leica EM SCD 50 evaporator. Conductivity and impedance measurements were performed in the range -40 °C to 220 °C with steps of 20 °C. Frequencies between 10 mHz to 10 MHz were applied using a Novocontrol Concept 80 broadband dielectric spectrometer. Due to a constant flow of nitrogen gas in a cryostat, the samples were tempered in dry N<sub>2</sub> atmosphere preventing the samples from further exposure with water or oxygen.

## 4. Results

In the following chapter all measured data are summarized for Ta-LLHO and Ta-LLSO, respectively.

### 4.1. $\text{Li}_{7-x}\text{La}_3\text{Hf}_{2-x}\text{Ta}_x\text{O}_{12}$ (Ta-LLHO)

For characterization of Ta-LLHO, DTA-TG, PXRD and EIS measurements were carried out. The results are given in the following subchapters.

#### 4.1.1. Differential Thermal Analysis Coupled with Thermogravimetry

Thermogravimetric analysis (TGA) was measured to analyze possible losses during heat treatment of the samples. To determine exothermic and endothermic changes during heating and cooling cycle, differential thermal analysis (DTA) was coupled. For screening, the calcinated 0.00 Ta-LLHO sample was taken. The resulting curves can be seen in Fig. 4.1.

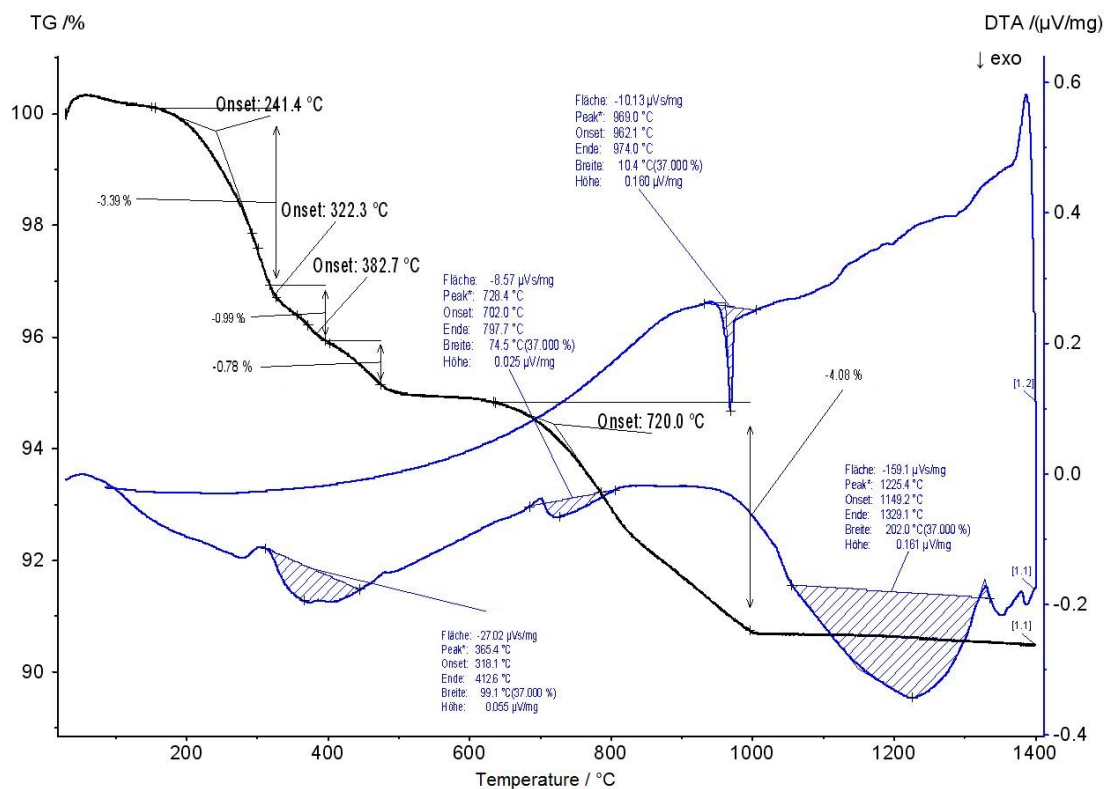
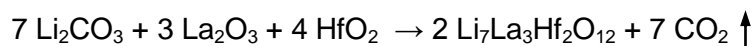


Fig. 4.1: Results of the DTA-TG measurement of the calcinated undoped LLHO sample. The arrows point to the onset and offset temperatures in the TG (black lines). The dashed lines denote the exothermic areas of the DTA (blue line).

Fig. 4.1 shows the result of the DTA-TG, which was measured for 0.00 Ta-LLHO. The black line represents the ratio of weight loss compared to the total mass of pestled and used powder. The blue line shows the exothermic and endothermic changes within the sample at given temperatures between 25 °C and 1400 °C. The black line shows four temperatures, where mass loss can be observed at onset temperatures of 241.4 °C, 322.3 °C, 382.7 °C and 720 °C, which sum up to a total mass loss of 9.3 % at 995 °C. At temperatures above 1000 °C only negligible losses could be further measured. The blue line reveals three exothermic processes with peak maxima measured at temperatures of 365 °C, 728 °C and 1225 °C in the heating process. Another sharp exothermic peak could be measured at 969 °C in the cooling process.

These exothermic processes indicate crystallization, phase transition or CO<sub>2</sub>-evaporation within the temperature range of the dotted area. Due to the fact that high losses occur up to 995 °C, the first and second exothermic peak can most likely be explained by CO<sub>2</sub>-evaporation, which did not completely evaporate during the calcination. Similar to reference [36], it is generated in the overall reaction:



Further losses were described as volatilization of Li<sub>2</sub>CO<sub>3</sub> at high temperatures by *Awaka et. al.* in 2009 and 2010. [12],[36],[37]

In the next step, PXRD measurements were carried out for determination of the crystal structure of the sintered products.

#### 4.1.2. X-Ray Diffraction

After the DTA-TG measurement, the first target was to synthesize single-phase crystals of undoped LLHO before doping of the garnet took place.

As described in chapter 3.1, 0.00 Ta-LLHO was pressed and heat treated at various temperatures at different holding times between 900 °C and 1230 °C on the basis of the methods used in literature. [13],[33],[36],[38] After the sintering process, X-ray powder pattern were recorded to be able to determine structural changes in the sample. The results were then compared with already known powder pattern of LLHO taken from the ICSD database to determine the crystal structure within the samples. Used temperatures and holding times in the sintering process are given in Tab. 4.1. The graphical representation can be seen in Fig. 4.2.

Tab. 4.1: Used temperatures and holding times in the sintering process for each LLHO sample.

Sample	1 <sup>st</sup> T [°C]	1 <sup>st</sup> holding time [h]	2 <sup>nd</sup> T [°C]	2 <sup>nd</sup> holding time [h]
LLHO_980C	900	5	980	5
LLHO_1000C	1000	12	-	-
LLHO_1050C	1000	5	1050	30
LLHO_1100C_unmilled	1100	24	-	-
LLHO_1100C_milled	1100	24	-	-
LLHO_1230	1200	0.25	1230	3.75

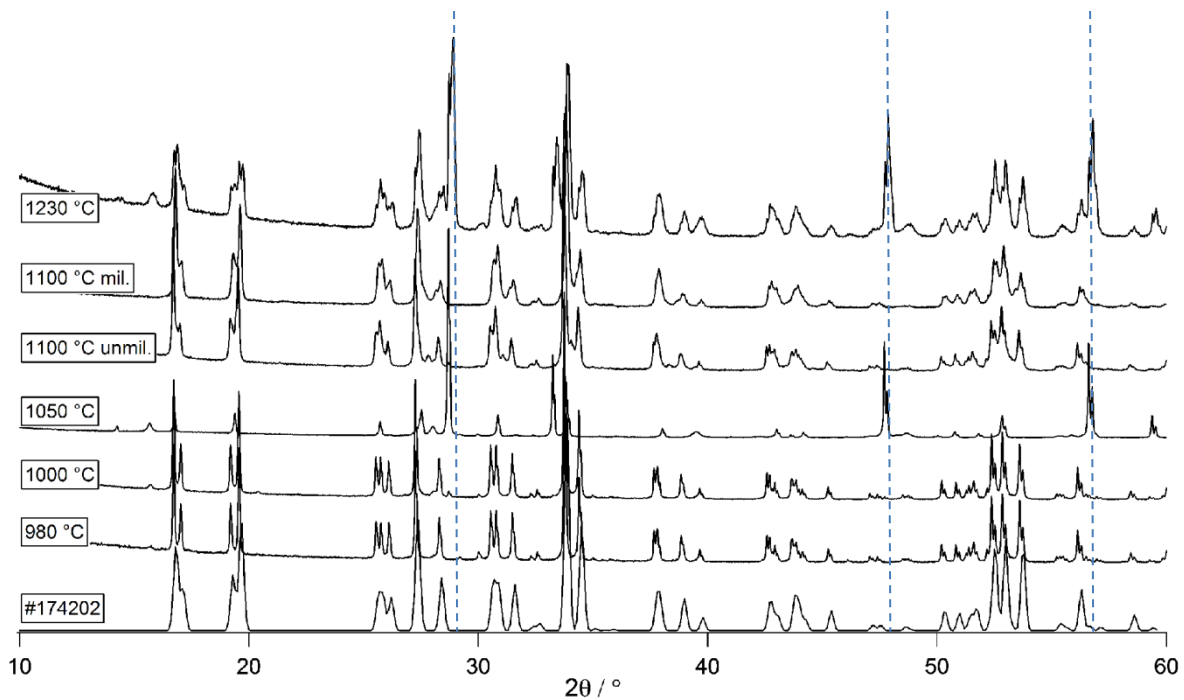
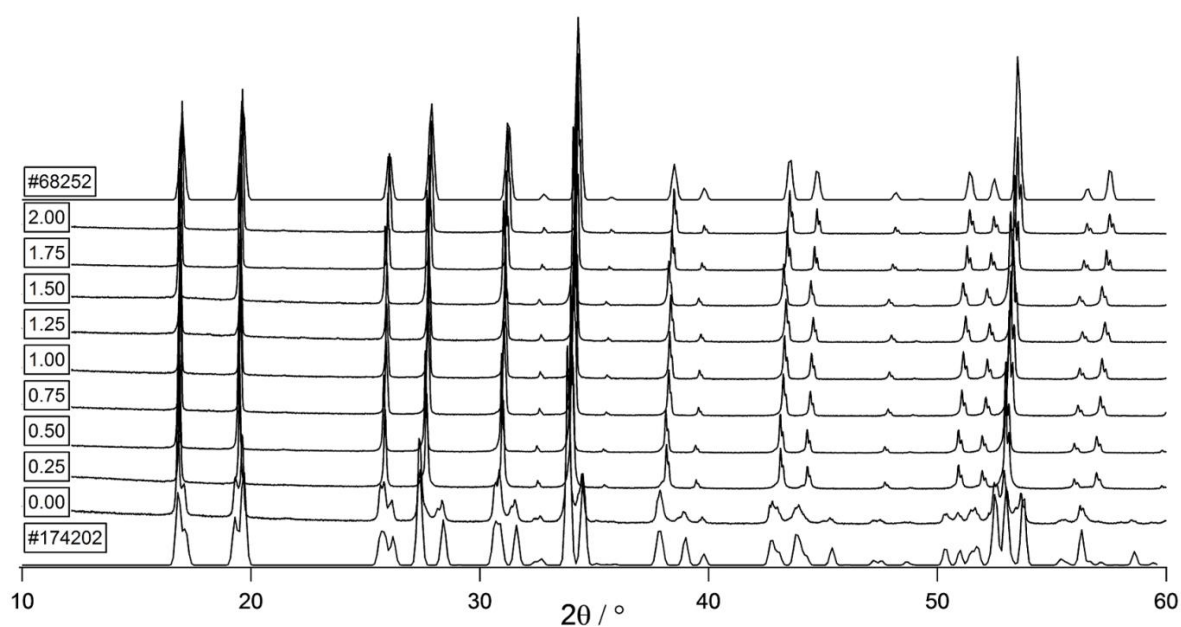


Fig. 4.2: X-ray powder pattern of 0.00 Ta-LLHO heat treated at various temperatures and holding times between 980 °C und 1230 °C with and without milling, prepared in air atmosphere. The blue dotted lines mark secondary phases. The reference was taken from the ICSD database and is used for comparison.

Fig. 4.2 shows the diffraction powder pattern of 0.00 Ta-LLHO sintered at various temperatures between 980 °C and 1230 °C and a reference of  $\text{Li}_7\text{La}_3\text{Hf}_2\text{O}_{12}$  with SG  $I4_1/acd$  (No. 142), taken from ICSD database (#174202). To determine the present phases and the symmetry of the garnets, data was collected in the range  $10^\circ \leq 2\theta \leq 60^\circ$ . The samples sintered at 980 °C and 1000 °C show high crystallinity. LLHO\_1050C, which was sintered for 35 h in total, and LLHO\_1230C, which was treated with the highest sintering temperature,

show dominant reflections at around  $28.7^\circ$ ,  $47.7^\circ$  and  $56.7^\circ$  (marked with blue dotted lines in Fig. 4.2). These reflections may be related to degradation of the samples due to Li loss, but further investigations would have to be made for exact determination. Compared to reference #174202, best results regarding highest crystallinity and lowest amount of mixed phases compared to the reference could be obtained, when the sample was heat treated at  $1100^\circ\text{C}$  for 24 h, as seen in LLHO\_1100C\_unmilled. The results could be further improved by ball milling, seen in LLHO\_1100C\_milled. Therefore, the sample preparation and heating program of LLHO\_1100C\_milled was further used for the synthesis of 0.00-2.00 Ta-LLHO. PXRD measurements were then carried out to detect differences in the crystal structure by increasing the amount of Ta.

In Fig. 4.3 the recorded diffraction powder pattern of differently doped Ta-LLHO in the range  $10^\circ \leq 2\theta \leq 60^\circ$  are displayed.



**Fig. 4.3: X-ray diffraction powder pattern of 0.00-2.00 Ta-LLHO series. References #68252 (cubic LLTO) and #174202 (tetragonal LLHO) were taken from ICSD database.**

Fig. 4.3 shows the diffraction powder pattern of 0.00-2.00 Ta-LLHO and references of LLHO with SG  $I4_1/acd$  (ICSD code #174202) and cubic  $\text{Li}_7\text{La}_3\text{Ta}_2\text{O}_{12}$  (LLTO) with SG  $Ia\bar{3}d$  (ICSD code #68252), respectively. 0.00 Ta-LLHO shows polycrystallinity with predominant tetragonal crystal structure. A change in the crystal structure from tetragonal to the cubic modification could be observed by increasing the amount to 0.25-2.00 Ta-LLHO yielding the SG  $Ia\bar{3}d$ . A Total shift of  $0.759^\circ$  from lower to higher values of  $2\theta$  can be seen related to increasing amounts of Ta leading to a decrease of the lattice parameter. This is caused by different ionic radii of Ta (78 pm) and Hf (85 pm). [19]

The lattice parameters of 0.00-2.00 Ta-LLHO are compiled in Tab. 4.2, showing linear behavior of cubic 0.25-2.00 Ta-LLHO in Fig. 4.4.

Tab. 4.2: Calculated unit cell parameters of 0.00 - 2.00 Ta-LLHO.

Composition	SG	Lattice parameter [Å]	Cell volume V [Å <sup>3</sup> ]
0.00 Ta-LLHO	$I4_1/acd$	a+b: 13.09500(58) c: 12.66722(67)	2172.16
0.25 Ta-LLHO	$Ia\bar{3}d$	a: 12.95294(18)	2173.23
0.50 Ta-LLHO	$Ia\bar{3}d$	a: 12.93235(17)	2162.88
0.75 Ta-LLHO	$Ia\bar{3}d$	a: 12.91179(15)	2152.58
1.00 Ta-LLHO	$Ia\bar{3}d$	a: 12.89143(17)	2142.41
1.25 Ta-LLHO	$Ia\bar{3}d$	a: 12.87337(20)	2124.38
1.50 Ta-LLHO	$Ia\bar{3}d$	a: 12.85515(19)	2133.42
1.75 Ta-LLHO	$Ia\bar{3}d$	a: 12.84278(11)	2118.25
2.00 Ta-LLHO	$Ia\bar{3}d$	a: 12.81884(14)	2106.43

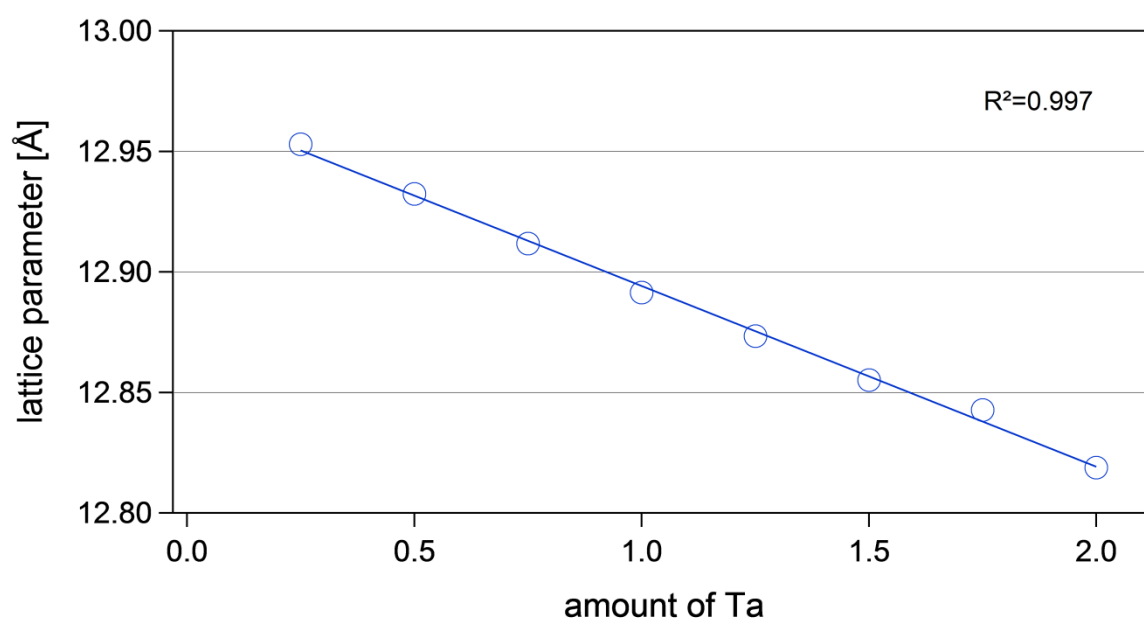


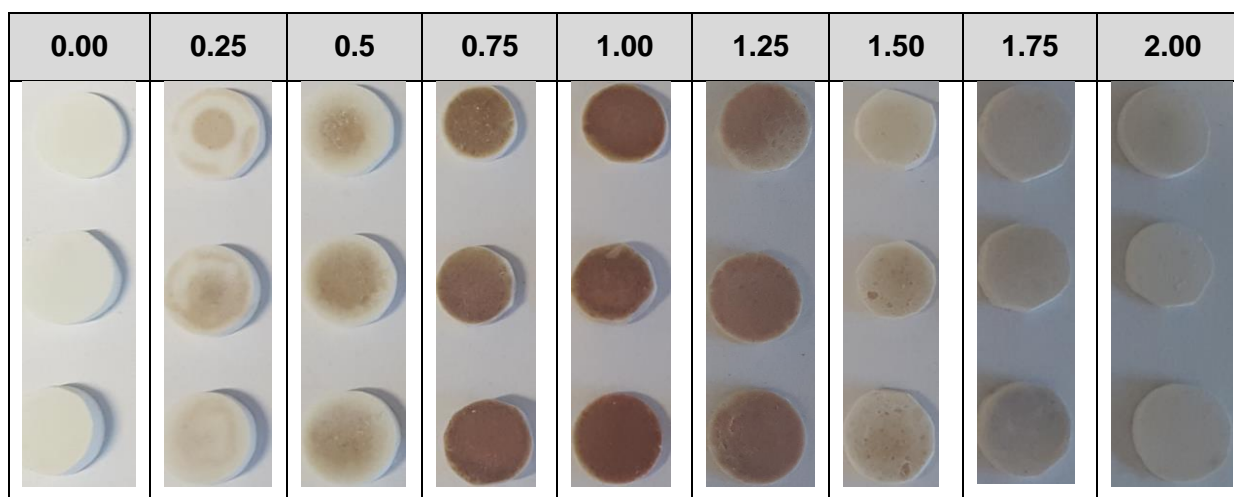
Fig. 4.4: Lattice parameter in dependency of Ta content in 0.25-2.00 Ta-LLHO. The blue line represents the fitting line with R<sup>2</sup>=0.997.

In Fig. 4.4, only cubic 0.25-2.00 Ta-LLHO samples are shown. 0.00 Ta-LLHO was skipped due to its tetragonal crystal structure. A linear dependency of the Ta content could be observed with decreasing lattice parameter from 12.95294(18) Å in 0.25 Ta-LLHO to 12.81884(14) Å in 2.00 Ta-LLHO. This causes a relative decreasing of the cell volume of approximately 3.1 % from 2173.23 Å<sup>3</sup> to 2106.43 Å<sup>3</sup>. However, the cell volume of tetragonal 0.00 Ta-LLHO is comparable to cubic 0.25 Ta-LLHO.

### 4.1.3. Dimensional Change after Sintering

After the sintering process, the sample colors changed from white to brown color. The most significant change could be observed for 1.00 Ta-LLHO, seen in Tab. 4.3. Further, relative shrinkage after the final sintering step was determined. The highest relative shrinkage (15.2 %) was found for 1.00 Ta-LLHO. The relative dimensional changes of all samples are given in Tab. 4.4.

Tab. 4.3: Optical change of 0.00-2.00 Ta-LLHO after sintering.



Tab. 4.4: Relative shrinkage of 0.00-2.00 Ta-LLHO after sintering.

Sample position	Ratio								
	0.00	0.25	0.50	0.75	1.00	1.25	1.50	1.75	2.00
Bottom	5.9	6.1	11.0	8.5	12.0	13.8	2.2	5.5	5.0
Middle	3.0	10.5	12.6	12.5	16.0	15.6	6.4	5.7	4.5
Top	6.0	11.1	11.5	16.4	18.2	15.2	7.4	9.0	5.0
<b>Mean values</b>	<b>5.0</b>	<b>9.2</b>	<b>11.7</b>	<b>12.5</b>	<b>15.4</b>	<b>14.9</b>	<b>5.3</b>	<b>6.7</b>	<b>4.8</b>
Standard deviation	1.39	2.23	0.67	3.23	2.57	0.77	2.25	1.60	0.24

The mean density  $\rho$  is given in Tab. 4.5. A graphical representation of the mean values of the density  $\rho$  and the relative pellet shrinkage in dependency of the Ta content is given in Fig. 4.5.

Tab. 4.5: Mean density of 0.00-2.00 Ta-LLHO after sintering.

Sample position	Ratio									
	0.00	0.25	0.50	0.75	1.00	1.25	1.50	1.75	2.00	
Mean density $\rho$ [g·cm <sup>-3</sup> ]	4.11	4.44	4.62	5.11	5.45	5.17	4.63	4.40	4.40	3.72
Standard deviation	0.11	0.05	0.04	0.07	0.06	0.5	0.19	0.29	0.29	0.04

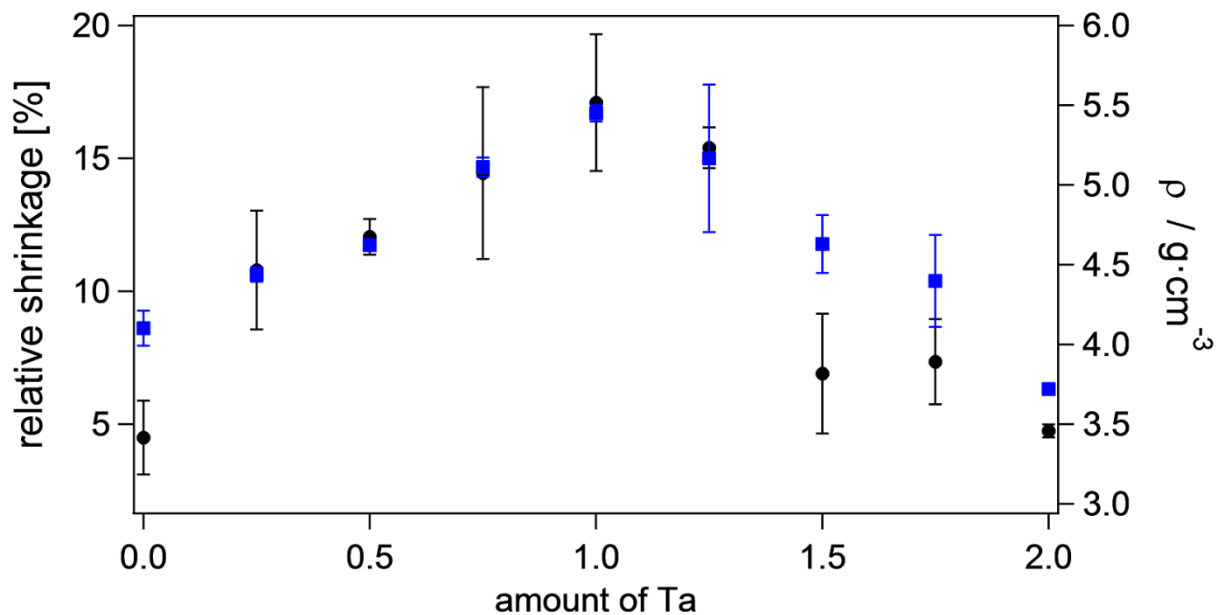


Fig. 4.5: Graphical representation of the density (blue squares) and relative shrinkage (black dots) of Ta-LLSO at different compositions. The error bars mark the standard deviation.

Depending on the composition, differences by means of the densification of the pellets were observed, leading to an increase of the relative shrinkage from ~4-17 % considering 0.00-1.00 Ta-LLHO. By further increasing the amount of Ta, relative densification decreases to ~4-7 %, comparable to pure 0.00 Ta-LLHO. No correlation with the calculated lattice parameters, given in Tab. 4.2, could be found. For some samples, the calculated standard deviation is very high (up to  $\pm 25.9$  %). The reason is that low relative shrinkage of the bottom samples compared to the middle and top samples could be observed. It leads to the assumption that the position in the ceramic crucible seems to influence the sintering step and thus the densification of the samples. Shielding of the temperature is assumed, which

creates a temperature gradient in the oven. Further, by taking a look at the pellets of 0.25 Ta-LLHO and 0.50 Ta-LLHO in Tab. 4.3, inhomogeneity regarding the brownish color on the inside and the white color on the outside of the pellets could be assumed.

Afterwards, the electrochemical properties by means of the conductivity  $\sigma$  and activation energy  $E_a$  were analyzed. Further, the influence of the microstructure on the ionic conductivity  $\sigma$  and the activation energy  $E_a$  should be investigated. Thus, EIS measurements were performed for 0.00-2.00 Ta-LLHO. The samples with the highest densification were used for the analysis.

#### 4.1.4. Electrical Studies

The data which is presented in the following subchapters were taken from milled 0.00 Ta-LLHO, which was sintered at 1100 °C for 24 h. If not stated elsewhere, it is used as an example for all EIS measurements, which were carried out for 0.00-2.00 Ta-LLHO.

To receive the conductivity isotherms for determining the  $\sigma_{DC}$ -plateaus at chosen temperatures, the real part of the conductivity  $\sigma'$  was plotted vs. the frequency  $\nu$  in a double-logarithmic scale, seen in Fig. 4.6.

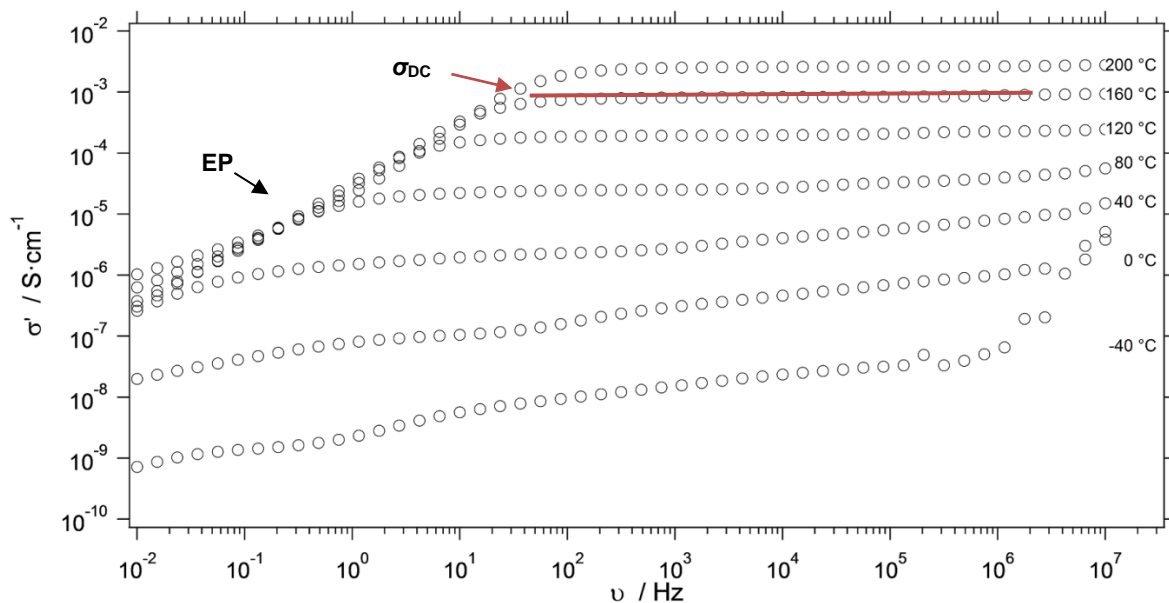


**Fig. 4.6:** Conductivity isotherms of 0.00 Ta-LLHO, sintered at 1100 °C for 24 h.  $\sigma'$  is plotted vs.  $\nu$  in the heating process of 0.00 Ta-LLHO. The red dotted line represents a  $\sigma_{DC}$ -plateau.

In Fig. 4.6, the real part of the conductivity  $\sigma'$  of the sample between -40 °C and 200 °C at selected frequencies can be seen. The figure shows typical EB at low frequencies and temperatures >40 °C. By increasing the frequency, conductivity isotherms appear. Two plateaus could be obtained at temperatures between -40 °C to 80 °C. By further increasing the temperature up to 200 °C, only one plateau is visible, because the resistance decreases

at increasing temperatures, shifting the bulk process to the high frequency region. Grain boundary processes show higher activation energies leading to a predominant signal at high temperatures. At temperatures between  $-40\text{ }^{\circ}\text{C}$  to  $20\text{ }^{\circ}\text{C}$ , dispersive regions were detected after increasing the frequency to  $>1\text{ MHz}$ . In this region, the real part of conductivity  $\sigma'$  is dependent on the frequency  $\nu$ . The first plateau at lower frequencies could only be observed in 0.00 Ta-LLHO with tetragonal modification. For cubic 0.25-2.00 Ta-LLHO, only the second plateau at higher frequencies was detected. This leads to the assumption that multiple processes contribute to the ionic conductivity within 0.00 Ta-LLHO caused by grain boundary  $\sigma_{\text{GB}}$  or bulk  $\sigma_{\text{bulk}}$  processes. For exact determination, the capacitance  $C$  at  $20\text{ }^{\circ}\text{C}$  was calculated by plotting the imaginary part of the impedance  $Z''$  vs. the real part of the impedance  $Z'$ , yielding the Nyquist plot (Fig. 4.7). The Nyquist plot represents the processes, which contribute to the electrical properties. These properties results from the bulk material, grain boundary effects or interfacial phenomena. [27] In Fig. 4.7, the Nyquist plot, observed from 0.00 Ta-LLHO at  $20\text{ }^{\circ}\text{C}$ , was compared to cubic 1.00 Ta-LLHO, also measured at  $20\text{ }^{\circ}\text{C}$ , to get a better understanding of the differences regarding the electrical properties. In Fig. 4.7b, 1.00 Ta-LLHO acts as a representative example for 0.25-2.00 Ta-LLHO, showing cubic modification.

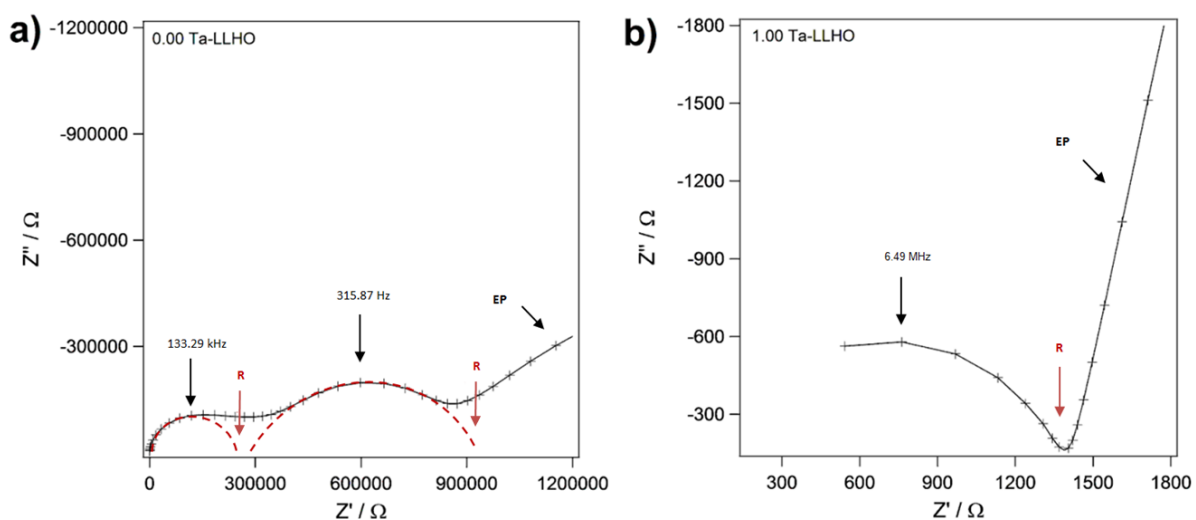


**Fig. 4.7:** Nyquist diagrams of a) polycrystalline 0.00 Ta-LLHO and b) cubic 1.00 Ta-LLHO measured at  $20\text{ }^{\circ}\text{C}$ . The red, dashed lines represent the fitted semicircles, observed by EIS measurements. The red arrows point to the intercept with the  $Z'$ -axis and the black arrows mark the maxima of the semicircles and to the area, where EP takes place, respectively.

In Fig. 4.7, the Nyquist plots of a) tetragonal 0.00 Ta-LLHO and b) cubic 1.00 Ta-LLHO, measured at  $20\text{ }^{\circ}\text{C}$ , are displayed. In a), two non-ideal semicircles were observed, followed by an increase of the imaginary part of the impedance  $Z''$  at low frequencies caused by EP. For determination of the ongoing processes at the predominant semicircles, the semiarcs

were fitted (red dashed lines) for the calculation of the capacities. In Fig. 4.7b, only one semicircle at high frequencies and a steady increase of the imaginary part of the impedance  $Z''$  at low frequencies was observed. To be able to relate the different regions to bulk or grain boundary processes, the capacitance  $C$  was introduced. The capacities for a) 0.00 Ta-LLHO is in the pF range at high frequencies. For lower frequencies it is falling into the order of  $10^{-9}$  F. For b) 1.00 Ta-LLHO, the capacitance  $C$  is 17.6 pF.

Taken all calculated data into account, the semicircle at low frequencies is attributed to grain boundary processes and the semiarc at higher frequencies denotes bulk processes. [39],[40] The intercepts with the  $Z'$ -axis, marked with the red arrows in Fig. 4.7, also correspond to the conductivity isotherms, seen in Fig. 4.6.

The conductivity can be calculated by the following equation:

$$\sigma' = \frac{1}{Z'} \cdot \frac{l}{A} \quad (4.2)$$

Here,  $\sigma'$  and  $Z'$  denote the real part of the conductivity and the real part of the impedance and  $l$  and  $A$  represent the thickness and the area of the pellet. [41] These result in a) 0.00 Ta-LLHO in a grain boundary conductivity  $\sigma_{GB}$  of  $5.50 \cdot 10^{-7} \text{ S} \cdot \text{cm}^{-1}$  and a bulk conductivity  $\sigma_{\text{bulk}}$  of  $1.56 \cdot 10^{-6} \text{ S} \cdot \text{cm}^{-1}$ . In b) 1.00 Ta-LLHO, a bulk conductivity  $\sigma_{\text{bulk}}$  of  $1.94 \cdot 10^{-4} \text{ S} \cdot \text{cm}^{-1}$  could be determined. The calculated bulk conductivities of 0.00-2.00 Ta-LLHO, determined at 20 °C, are summarized in Tab. 4.6.

Afterwards, the activation energy  $E_a$  of the bulk process was calculated by the following relation

$$\sigma' = \sigma_0 \cdot e^{-\frac{E_a}{k_B T}}, \quad (4.3)$$

showing Arrhenius-type behavior. The activation energy gives the amount of energy that is needed for a successful jump of the atom. Thus, low activation energies are usually related to high conductivities. [42] Therefore,  $\log(\sigma)$  is plotted vs.  $1000 \cdot T^{-1}$ . For 0.00 Ta-LLHO an activation energy  $E_a$  of 0.49(1) eV was calculated for the bulk process. The activation energy for the GB process is 0.57(1) eV. A graphical representation can be seen in Fig. 4.8.

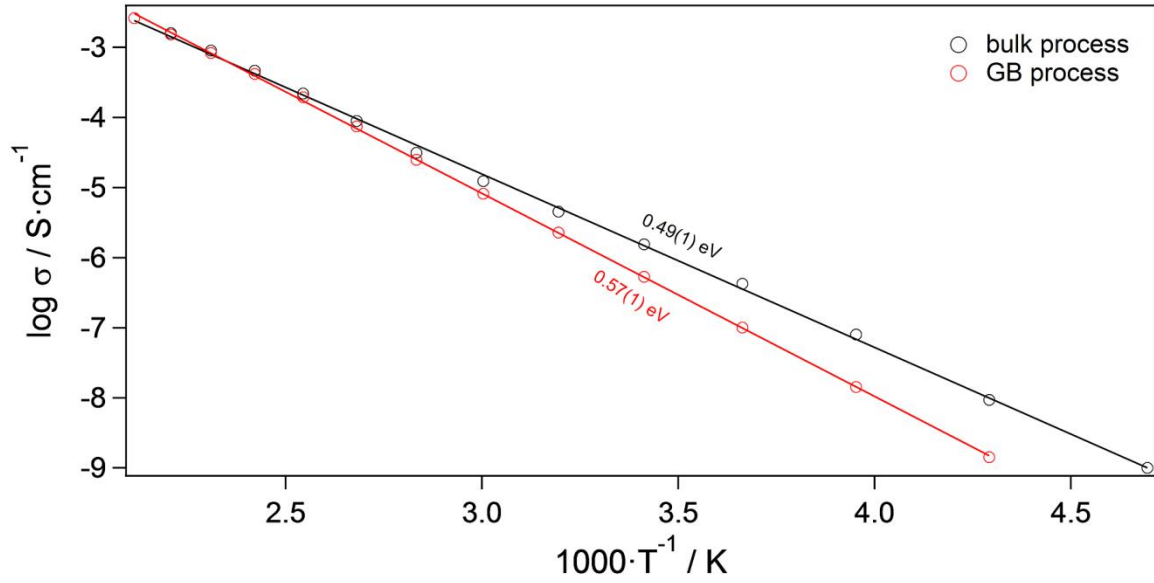


Fig. 4.8: Arrhenius plot of the bulk and GB process of 0.00 Ta-LLHO, calculated from the conductivity at the intercept with Z'-axis of the semicircle. The black and red lines represent the fitting lines, which were used for the determination of the activation energies  $E_a$ .

In Fig. 4.9, the collected data of the bulk process of every milled mixture of 0.00-2.00 Ta-LLHO are displayed showing non-linear behavior above 100 °C for 0.25-1.00 Ta-LLHO. The bulk conductivities  $\sigma_{\text{bulk}}$ , calculated for 20 °C, the activation energies  $E_a$  and the prefactors  $K$ , which were calculated from the fitting lines of each composition in a temperature range, where linear behavior could be observed, are presented in Tab. 4.6.

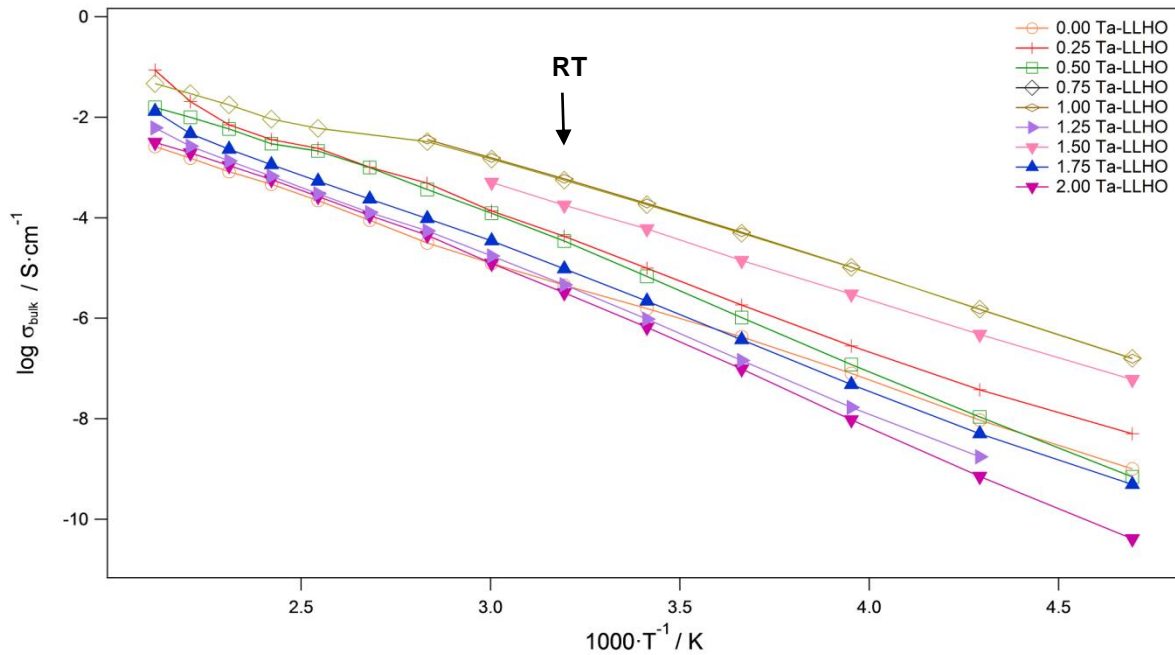


Fig. 4.9: Arrhenius plots of 0.00-2.00 Ta-LLHO. The lines between the dots serve as guide to the eye.

Tab. 4.6: Calculated bulk conductivities and activation energies of 0.00-2.00 Ta-LLHO.

Composition	$\sigma_{\text{bulk}}$ at 20 °C [S·cm <sup>-1</sup> ]	$E_a$ [eV]	log(K) [s <sup>-1</sup> ]
0.00 Ta-LLHO	$1.56 \cdot 10^{-6}$	0.490(4)	2.61
0.25 Ta-LLHO	$9.89 \cdot 10^{-6}$	0.532(7)	4.34
0.50 Ta-LLHO	$6.80 \cdot 10^{-6}$	0.608(6)	4.57
0.75 Ta-LLHO	$1.82 \cdot 10^{-4}$	0.461(5)	4.15
1.00 Ta-LLHO	$1.93 \cdot 10^{-4}$	0.466(5)	4.26
1.25 Ta-LLHO	$6.01 \cdot 10^{-5}$	0.484(6)	4.07
1.50 Ta-LLHO	$9.73 \cdot 10^{-7}$	0.610(8)	3.70
1.75 Ta-LLHO	$2.20 \cdot 10^{-6}$	0.566(5)	4.03
2.00 Ta-LLHO	$6.62 \cdot 10^{-7}$	0.614(9)	4.26

For tetragonal LLHO, a bulk conductivity of  $\sigma_{\text{bulk}}=1.56 \cdot 10^{-6} \text{ S} \cdot \text{cm}^{-1}$  could be observed, which matches quite well with the results found in literature ( $\sigma_{\text{bulk}}=9.85 \cdot 10^{-7} \text{ S} \cdot \text{cm}^{-1}$ ). [36] The change in the structure from tetragonal 0.00 Ta-LLHO to cubic 0.25 Ta-LLHO increases the bulk Li-ion conductivity from  $1.56 \cdot 10^{-6} \text{ S} \cdot \text{cm}^{-1}$  to  $9.89 \cdot 10^{-6} \text{ S} \cdot \text{cm}^{-1}$ . Cubic 0.50 Ta-LLHO shows a lower conductivity and higher activation energy than 0.25 Ta-LLHO, which could be related to inhomogeneity, seen in Tab. 4.3. By increasing the amount of Ta from 0.25 to 1.00 Ta-LLHO, the bulk conductivity  $\sigma_{\text{bulk}}$  increases by more than one order of magnitude from  $9.89 \cdot 10^{-6} \text{ S} \cdot \text{cm}^{-1}$  to  $1.93 \cdot 10^{-4} \text{ S} \cdot \text{cm}^{-1}$  at RT, leading to a decrease of the activation energy  $E_a$  from 0.538(4) eV to 0.466(5) eV. By further increasing the amount of Ta to completely exchanged Hf, the bulk conductivity  $\sigma_{\text{bulk}}$  decreases to  $6.62 \cdot 10^{-7} \text{ S} \cdot \text{cm}^{-1}$  with a calculated activation energy  $E_a$  of 0.614(9) eV. This may be related to an increasing amount of Ta and thus a decreasing amount of Hf and Li, causing a composition depending change of the charge carriers present (e.g. 6 Li atoms per unit in 1.00 Ta-LLHO compared to 5 Li atoms in 2.00 Ta-LLHO). Further, an increased ionic conductivity could be calculated of up to two orders of magnitude comparing the high conductive cubic (determined in 0.75 Ta-LLHO) and the low conductive tetragonal (found in 0.00 Ta-LLHO) modification.

By comparing the results with the mean relative shrinkage, seen in Tab. 4.4, it is assumed that the densification of the samples are somehow related to ionic conductivity, because the highest relative shrinkage (15.4 %), the best ionic conductivity ( $\sigma_{\text{bulk}}=1.93 \cdot 10^{-4} \text{ S} \cdot \text{cm}^{-1}$ ) and

the second lowest activation energy ( $E_a=0.466(5)$  eV) were found in 1.00 Ta-LLHO. All samples, which showed lower densification, showed much lower values for conductivity and higher activation energies. This is caused because more grain boundaries are present at lower densification leading to a higher resistance. However, no relation could be found regarding high values of bulk conductivities and low activation energies.

## 4.2. $\text{Li}_{7-x}\text{La}_3\text{Sn}_{2-x}\text{Ta}_x\text{O}_{12}$ (Ta-LLSO)

For the characterization of the behavior of undoped LLSO at different temperatures, again, a DTA-TG measurement was performed. PXRD patterns were recorded for obtaining the phases within the samples and EIS measurements were carried out to analyze the electrical properties of doped Ta-LLSO garnets. For all measuring techniques, the same procedures were used for Ta-LLSO as for Ta-LLHO. The results are given in the following subchapters.

### 4.2.1. Differential Thermal Analysis Coupled with Thermogravimetry

To make any losses of the material during heat treatment visible, DTA-TG was measured. The graphical representation of both TGA and DTA measurements are given in Fig. 4.10.

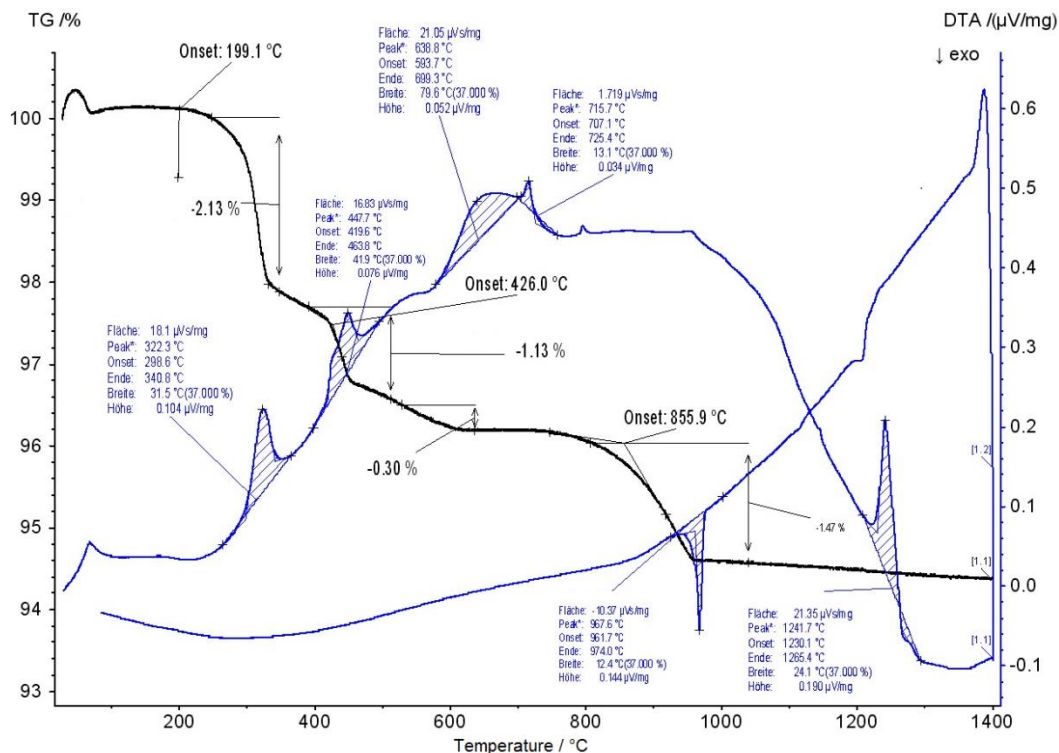
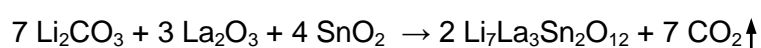


Fig. 4.10: Results of the DTA-TG measurement of the calcinated, undoped LLSO sample. The arrows point to the onset and offset temperatures in the TGA (black lines). The dashed lines denote the exothermic areas of the DTA (blue line).

Fig. 4.10 shows the result of the DTA-TG of 0.00 Ta-LLSO. The blue line shows the exothermic and endothermic changes within the powder at temperatures between 25 °C and 1400 °C. The black line represents the ratio of weight loss compared to the total mass of pestled and used sample. Looking at the black line, four temperatures were found, where mass loss occurs. The onset temperatures, where higher losses could be noticed, were determined at 199.1 °C, 426.0 °C and 855.9 °C. The total mass loss sums up to 5.4 % at 960 °C. At temperatures above 960 °C only negligible losses could be further detected.

The blue line shows three exothermic processes with peak maxima at temperatures of 365 °C, 728 °C and 1225 °C in the heating process. Another sharp exothermic peak was observed at 969 °C in the cooling process. These exothermic processes indicate crystallization, phase transition, CO<sub>2</sub>-evaporation or volatilization of Li<sub>2</sub>CO<sub>3</sub> at high temperatures within the dotted area. [36],[37] Due to the fact that high losses occur up to 995 °C, the first and second exothermic peak can most likely be explained by Li<sub>2</sub>CO<sub>3</sub> volatilization or CO<sub>2</sub>-evaporation, which did not completely evaporate during the calcination. Comparable to reference [36], it is generated in the overall reaction:



In the next step, PXRD measurements were carried out for determination of the crystal structure of the sintered products.

#### 4.2.2. X-Ray Diffraction

Analogue to 0.00 Ta-LLHO in chapter 4.1.2, it was tried to synthesize single-phase crystals of undoped LLSO before compositions of 0.00-2.00 Ta-LLSO samples were prepared.

Therefore, undoped LLSO was pressed and heat treated between 850 °C and 1230 °C on the basis of the heating program used for LLHO and the literature. [35] Later, PXRD measurements were carried out for determining structural changes in the sample. The observed reflections were then compared with two references (#163914 and #237808, showing tetragonal, SG:  $I4_1/acd$ , and cubic, SG:  $Ia\bar{3}d$ , crystal structure, respectively), taken from ICSD database. Used temperatures and holding times in the sintering process are given in Tab. 4.7. The observed diffraction powder pattern can be seen in Fig. 4.11.

Tab. 4.7: Used temperatures and holding times in the sintering process for each LLSO sample.

Sample	1 <sup>st</sup> T [°C]	1 <sup>st</sup> holding time [h]	2 <sup>nd</sup> T [°C]	2 <sup>nd</sup> holding time [h]
LLSO_850	850	12	-	-
LLSO_900	900	12	-	-
LLSO_1000C	1000	5	1000	5
LLSO_1100C	1100	5	-	-
LLSO_1100C_milled	1100	24	-	-
LLSO_1230	1200	0.25	1230	3.75

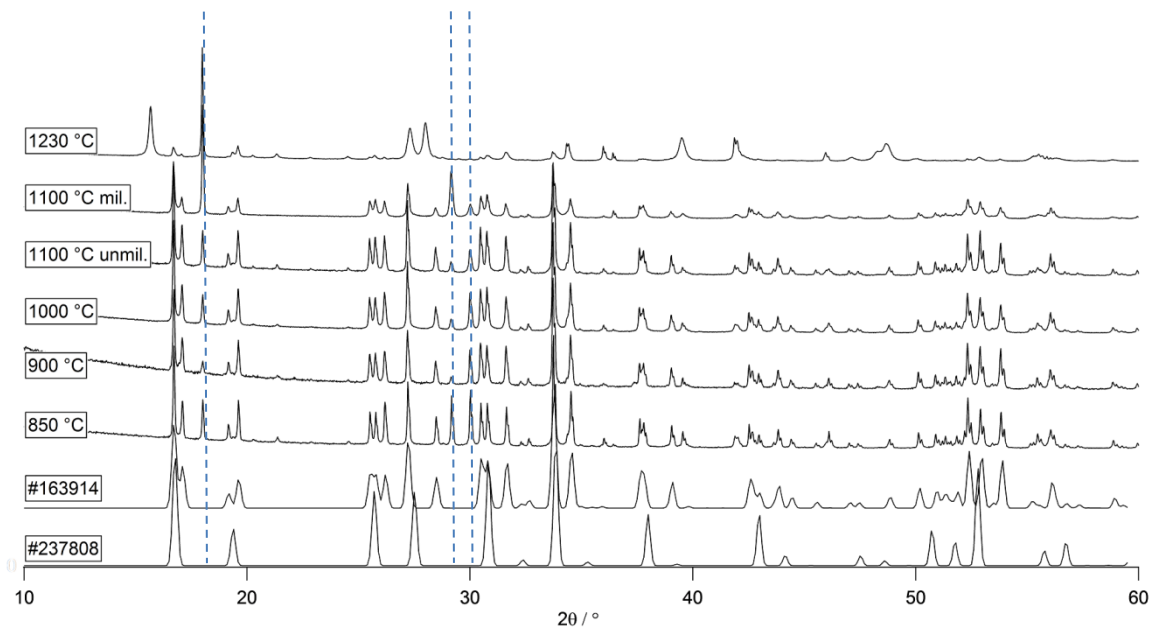


**Fig. 4.11: X-ray powder pattern of 0.00 Ta-LLSO heat treated at various temperatures and holding times between 850 °C and 1230 °C with and without milling, prepared in air atmosphere. The blue dotted lines mark secondary phases. The references were taken from the ICSD database and are used for comparison.**

Comparing the results with the references found in the ICSD database, it can be seen in Fig. 4.11 that independent of the sintering time only LLSO with tetragonal crystal structure between 850 °C and 1100 °C could be synthesized. For LLSO sintered at 1230 °C, it is assumed that degradation takes place as seen in undoped LLHO in Fig. 4.2 in chapter 4.1.2. Between 850 °C and 1100 °C, three reflections (marked with blue dotted lines in Fig. 4.11) at 18.0 °, 29.2 ° and 30.0 ° were detected that could be related to  $\text{Li}_2\text{SnO}_3$  (ICSD code #21032 with SG:  $C 1 2/c 1$ , No. 15). However, in dependency of LLHO, the same procedure and heat treatment was used for the synthesis of 0.00-2.00 Ta-LLSO.

The recorded diffraction powder pattern of sintered 0.00-2.00 Ta-LLSO can be seen in Fig. 4.12.

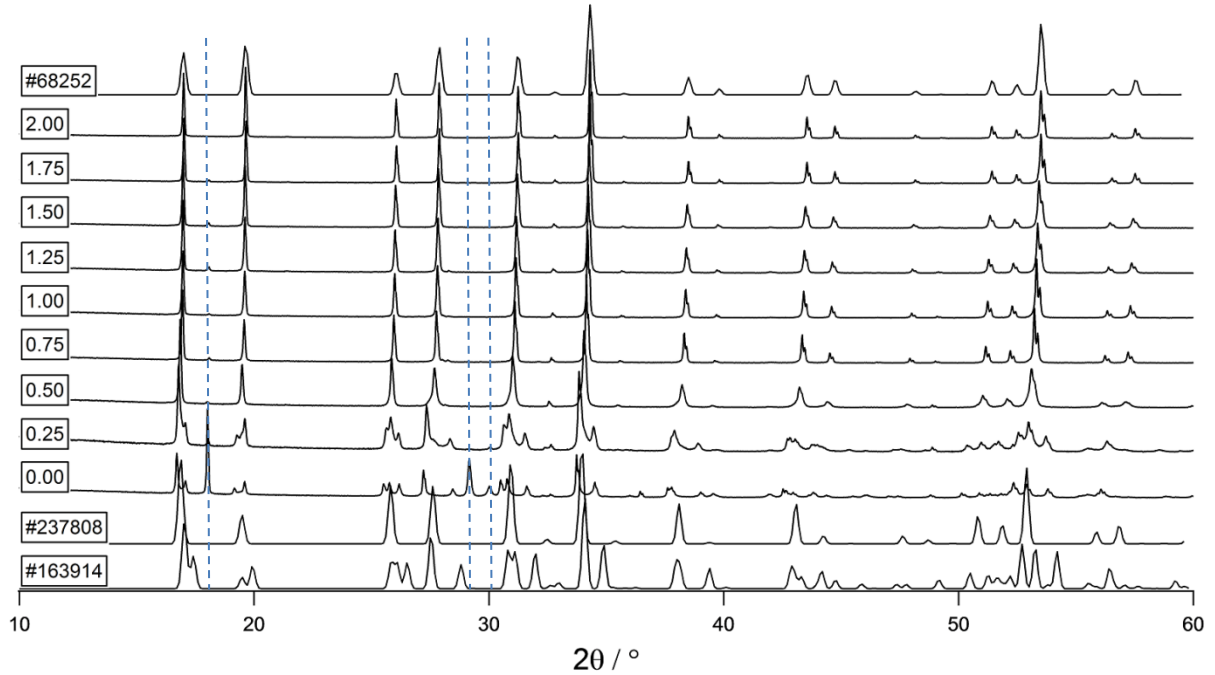


**Fig. 4.12: X-ray diffraction pattern of 0.00-2.00 Ta-LLSO series. The blue dotted lines represent secondary phases. References #68252 (cubic LLTO) as well as #237808 (cubic modification) and #163914 (tetragonal modification) were taken from ICSD database.**

Fig. 4.12 shows the diffraction powder pattern of 0.00 – 2.00 Ta-LLSO and references of  $\text{Li}_7\text{La}_3\text{Sn}_2\text{O}_{12}$  with SG  $I4_1/acd$  (ICSD code #163914) and  $Ia\bar{3}d$  (ICSD code #237808), respectively, and cubic LLTO with SG  $Ia\bar{3}d$  (ICSD code #68252). 0.00-0.25 Ta-LLSO show polycrystallinity with predominant tetragonal crystal structure. Two reflections found at  $29.2^\circ$  and  $30.0^\circ$  completely disappear when increasing the amount of Ta in the samples. Up to 1.75 Ta-LLSO, the third reflection, found at  $18.0^\circ$  (marked with a blue dotted line in Fig. 4.12), according to the secondary phase  $\text{Li}_2\text{SnO}_3$ , is still present. A change in the crystal structure from tetragonal to cubic modification could be observed by increasing the amount of Ta from 0.00 to 0.50-2.00 Ta-LLSO yielding the garnet-type structure  $Ia\bar{3}d$ . A total shift of  $0.8812^\circ$  from lower to higher values of  $2\theta$  can be seen related to increasing amounts of Ta, which has a smaller ionic radius than Sn (78 pm compared to 83 pm). [19] This difference leads to decreasing lattice parameter of the unit cells with decreasing amounts of Sn. The lattice parameters of 0.00-2.00 Ta-LLSO are given in Tab. 4.8. By plotting the lattice parameter vs. the Ta content, a linear behavior of decreasing unit cell parameters to decreasing amount of Sn could be observed, seen in Fig. 4.13.

Tab. 4.8: Lattice parameter of 0.00-2.00 Ta-LLSO.

Composition	SG	Lattice parameter [Å]	Cell volume V [Å <sup>3</sup> ]
0.00 Ta-LLSO	$I4_1/acd$	a+b: 13.11917(76) c: 12.56190(87)	2162.06
0.25 Ta-LLSO	$I4_1/acd$	a+b: 13.06280(68) c: 12.63517(77)	2156.07
0.50 Ta-LLSO	$Ia\bar{3}d$	a: 12.90240(30)	2147.89
0.75 Ta-LLSO	$Ia\bar{3}d$	a: 12.89057(10)	2141.99
1.00 Ta-LLSO	$Ia\bar{3}d$	a: 12.86934(14)	2131.42
1.25 Ta-LLSO	$Ia\bar{3}d$	a: 12.85548(14)	2124.54
1.50 Ta-LLSO	$Ia\bar{3}d$	a: 12.84028(16)	2117.01
1.75 Ta-LLSO	$Ia\bar{3}d$	a: 12.82447(13)	2109.20
2.00 Ta-LLSO	$Ia\bar{3}d$	a: 12.81884(14)	2106.43

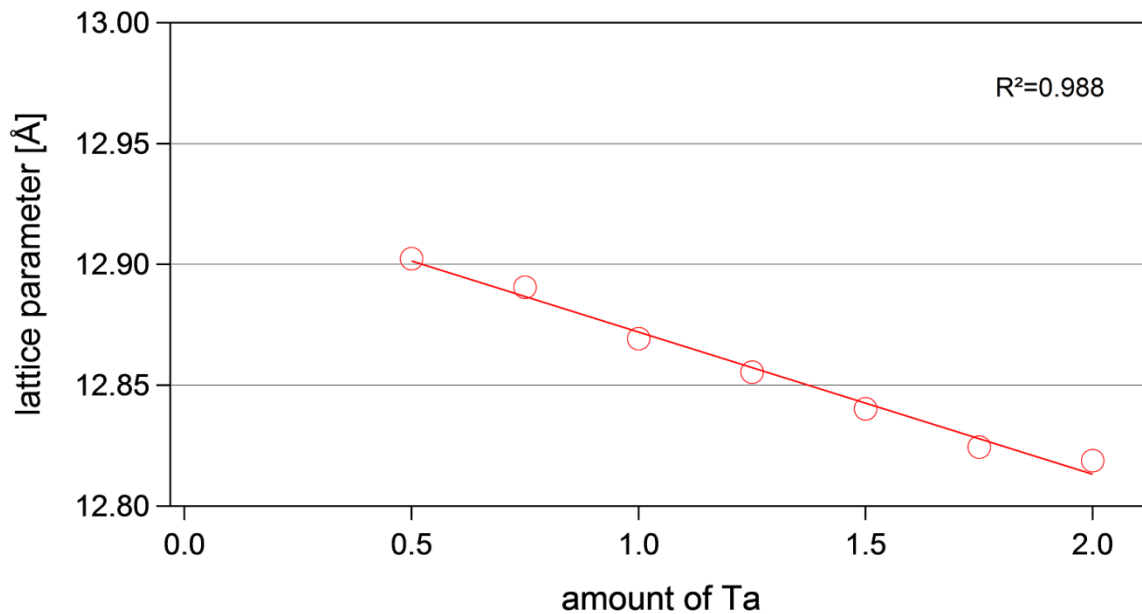


Fig. 4.13: Lattice parameters in dependency of Ta content in 0.50-2.00 Ta-LLSO. The red line represents the fitting line with R<sup>2</sup>=0.988.

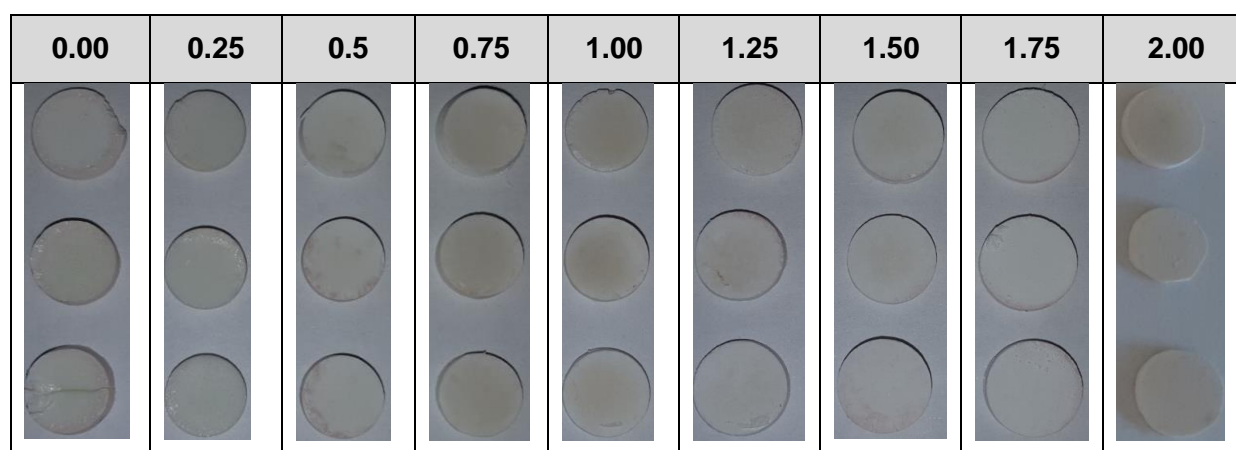
In Fig. 4.13, cubic 0.50-2.00 Ta-LLSO is displayed. 0.00-0.25 Ta-LLSO were not included into the figure, because they have a tetragonal crystal structure and therefore a different

symmetry of the unit cell. However, for 0.50-2.00 Ta-LLSO, decreasing lattice parameter with increasing amounts of Ta could be observed (12.90240(30) Å to 12.81884(14) Å) summing up to a relative decreasing cell volume of approximately 1.9 % from 2147.89 Å<sup>3</sup> to 2106.43 Å<sup>3</sup>. For 0.00 Ta-LLSO and 0.25 Ta-LLSO, the cell volumes were determined as 2162.06 Å<sup>3</sup> and 2156.07 Å<sup>3</sup>, respectively.

### 4.2.3. Dimensional Change after Sintering

Although the change of the color for differently doped Ta-LLSO is not as conspicuous as in Ta-LLHO (seen in Tab 4.3 in chapter 4.1.3), a slight difference of the pellets can still be noticed, seen in Tab. 4.9. The relative dimensional shrinkage of the samples is given in Tab. 4.10.

Tab. 4.9: Optical change of 0.00-2.00 Ta-LLSO after sintering.



Tab. 4.10: Relative shrinkage of 0.00-2.00 Ta-LLSO after sintering.

Sample position	Ratio								
	0.00	0.25	0.50	0.75	1.00	1.25	1.50	1.75	2.00
Bottom	4.9	15.6	13.6	8.0	13.6	5.2	-2.6	-2.1	5.0
Middle	13.6	14.1	14.6	14.0	12.0	3.4	-0.1	-1.7	4.5
Top	11.1	17.1	14.6	15.2	8.6	-1.1	-2.6	-1.7	5.0
<b>Mean value</b>	<b>9.9</b>	<b>13.3</b>	<b>14.3</b>	<b>12.4</b>	<b>11.4</b>	<b>2.5</b>	<b>-1.8</b>	<b>-1.8</b>	<b>4.8</b>
Standard deviation	3.7	1.0	0.5	3.1	2.1	2.6	1.2	0.2	0.2

The density  $\rho$  is given in Tab. 4.11. A graphical representation of the mean values of the calculated density and relative pellet shrinkage is given in Fig. 4.14.

Tab. 4.11: Mean density of 0.00-2.00 Ta-LLSO after sintering.

Sample position	Ratio								
	0.00	0.25	0.50	0.75	1.00	1.25	1.50	1.75	2.00
Mean density $\rho$ [ $\text{g}\cdot\text{cm}^{-3}$ ]	4.24	4.74	4.54	4.40	4.25	3.21	3.10	2.98	3.72
Standard deviation	0.39	0.05	0.19	0.34	0.28	0.21	0.02	0.01	0.04

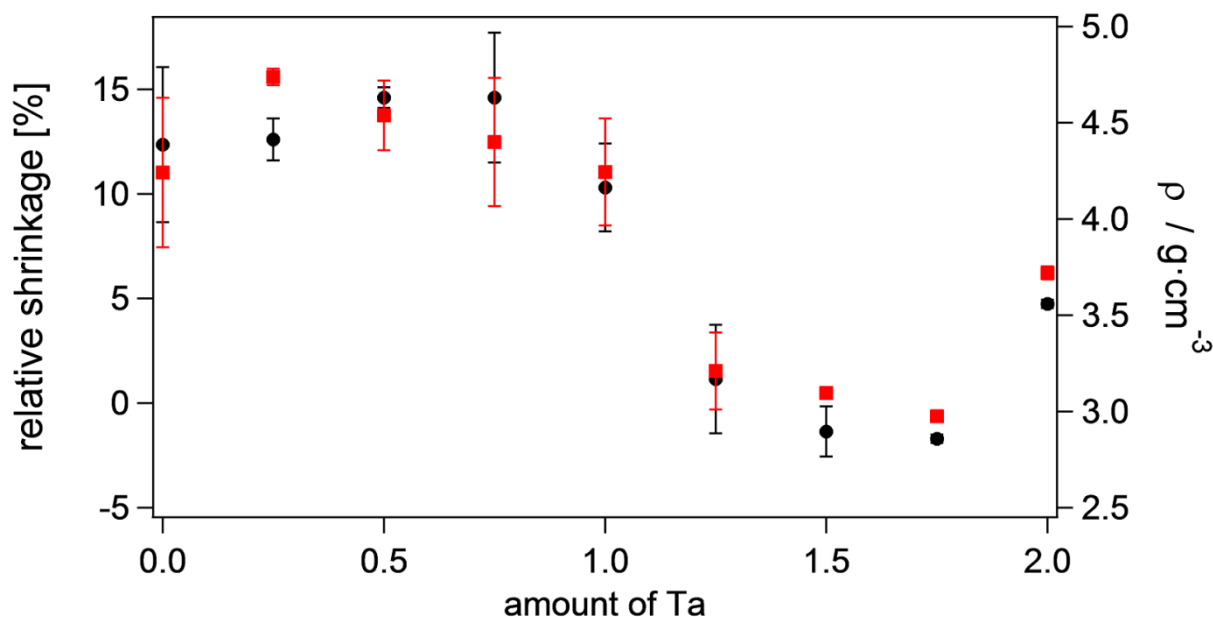


Fig. 4.14: Graphical representation of the density (red squares) and relative shrinkage (black dots) of Ta-LLSO at different compositions. The error bars mark the standard deviation.

Tab. 4.10 and Fig. 4.14 reveal high values of densification found for 0.00-1.00 Ta-LLSO with a relative shrinkage ranging from 9 to 16 % and densities  $\rho$  between 4.2-4.8  $\text{g}\cdot\text{cm}^{-3}$ . By further increasing the amount of Ta, the relative shrinkage and density decrease to 4 % and 3.72  $\text{g}\cdot\text{cm}^{-3}$  for 2.00 Ta-LLSO. For 1.25-1.75 Ta-LLSO, an increasing diameter to 2 % was found. Considering the calculated lattice parameters, given in Tab. 4.8, no correlation with the relative shrinkage and density, respectively, could be found. The high standard deviation can be explained by the position of the pellets in the ceramic crucible as the samples, which were placed at the bottom, show much lower relative shrinkage than the middle and bottom samples indicating that, as for LLHO, the position in the oven and in the crucible, respectively, influences the sintering step.

Analogue to Ta-LLHO, the electrochemical processes were studied. Thus, EIS measurements were carried out for 0.00-2.00 Ta-LLSO. Always the samples with highest densification were analyzed.

#### 4.2.4. Electrical Studies

As for LLHO, a temperature range of -40 °C to 200 °C was set for the EIS measurements. The following figures in this chapter were taken from milled 0.00 Ta-LLSO, which was sintered at 1100 °C for 24 h. If not stated elsewhere, it serves as a representative example for all EIS measurements that were carried out for 0.00-2.00 Ta-LLSO.

At first, the real part of the conductivity  $\sigma'$  was plotted vs. the frequency  $\nu$  in a double-logarithmic scale to obtain the conductivity isotherms, seen in Fig. 4.15.

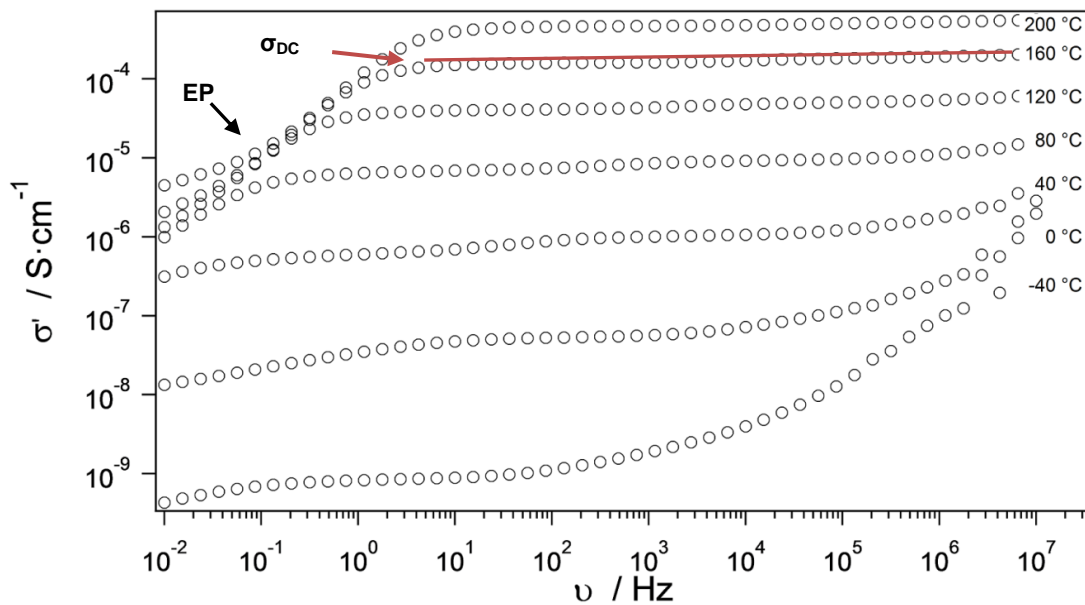
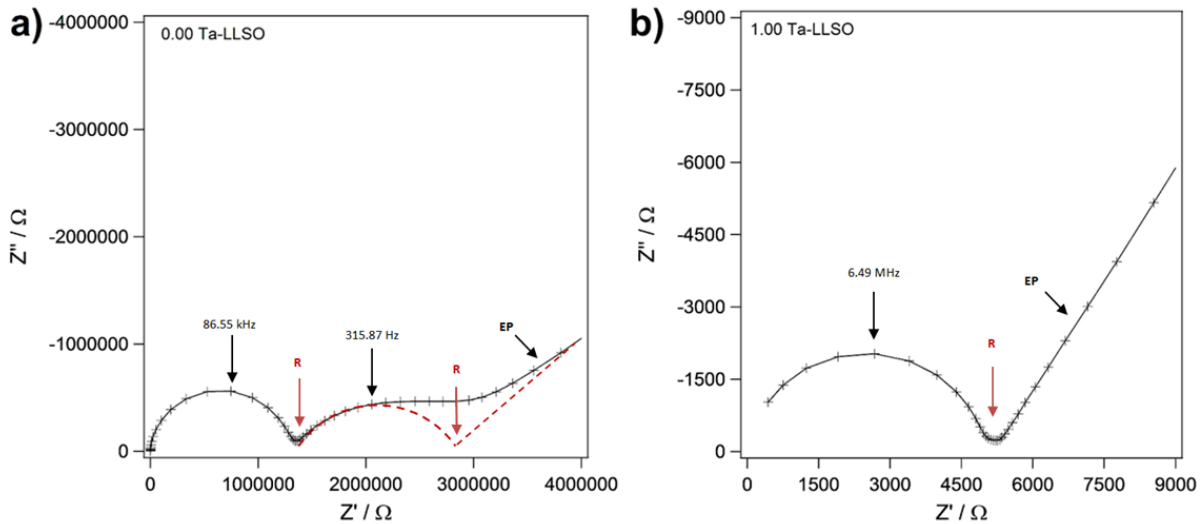


Fig. 4.15: Real part of the conductivity  $\sigma'$  vs. the frequency  $\nu$  of 0.00 Ta-LLSO at selected temperatures. The red line represents a  $\sigma_{DC}$ -plateau.

Fig. 4.15 reveals typical EB at low frequencies and high temperatures. By increasing the frequency, distinct conductivity plateaus appear. For exact determination if grain boundary, bulk or interface processes are related to those isotherms, the capacitance  $C$  was calculated. Therefore, the imaginary part of the impedance  $Z''$  was plotted vs. the real part of impedance  $Z'$ , yielding the Nyquist plot. As for LLHO, a graphical representation of the Nyquist diagrams of 0.00 Ta-LLSO and 1.00 Ta-LLSO, measured at 20 °C, are given in Fig. 4.16 to reveal differences between the tetragonal and cubic modification.



**Fig. 4.16:** Nyquist plots of a) polycrystalline 0.00 Ta-LLSO and b) cubic 1.00 Ta-LLSO measured at 20 °C. The red, dashed lines represent the fitted semicircles, observed by EIS measurements. The red arrows point to the intercept with the  $Z'$ -axis and the black arrows mark the maxima of the semicircles and to the area, where EP takes place, respectively.

Fig. 4.16a shows the Nyquist plot of 0.00 Ta-LLSO, revealing two semicircles. The second semicircle at lower frequencies shows overlapping with other signals, indicating other semicircles and therefore other relaxation processes. This assumption is supported by the fact that other unidentified reflections were found in the PXRD measurement (Fig. 4.12). For exact determination, further investigations would have to be made. However, the second semicircle was fitted (red dashed semicircle in Fig. 4.16a) to determine the intercept with the  $Z'$ -axis of the signal. In Fig. 4.16b, the Nyquist plot of 1.00 Ta-LLSO is displayed, showing only one semicircle at much higher frequencies compared to 0.00 Ta-LLSO.

The capacitance  $C$  for the first semicircle at high frequencies in a) 0.00 Ta-LLSO is 7.73 pF and the values for the second fitted semicircle at low frequencies is  $3.64 \cdot 10^{-9}$  F. The semicircles can therefore be related to bulk and grain boundary processes, respectively. The semicircle seen in Fig. 4.16b is in the range of pF and can be related to bulk processes.

The activation energies of the GB and bulk processes of 0.00-2.00 Ta-LLSO were calculated as in chapter 4.1.4. The activation energies of the GB processes of 0.00 Ta-LLSO and 0.25 Ta-LLSO are 0.54(1) eV and 0.39(2) eV (compared to 0.52 eV and 0.38 eV for the bulk processes of the corresponding samples) with  $\log(K_{0.00})=2.44 \text{ s}^{-1}$  and  $\log(K_{0.25})=2.30 \text{ s}^{-1}$ . For the determination of the activation energies of the bulk processes of all samples,  $\log(\sigma_{\text{bulk}})$  is plotted vs.  $1000 \cdot T^{-1}$ . The Arrhenius diagrams of all Ta doped LLSO samples are displayed in Fig. 4.17. The calculated activation energies  $E_a$  and prefactors  $K$ , calculated from the fitting lines, where linear behavior could be observed, are summarized in Tab. 4.12.

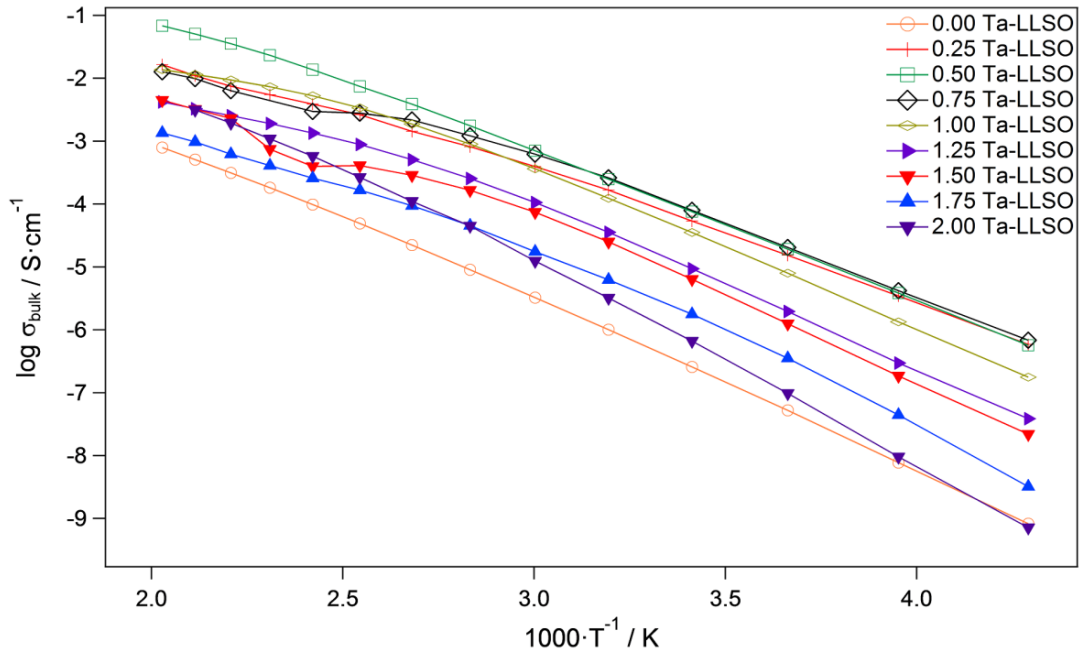


Fig. 4.17: Arrhenius diagram of the 0.00-2.00 Ta-LLSO. The lines between the dots serve as guide to the eye.

Fig. 4.17 shows the Arrhenius diagram of 0.00-2.00 Ta-LLHO. 0.00 Ta-LLHO shows a linear Arrhenius behavior. For 0.25-2.00 Ta-LLHO, a slight drop of  $\log(\sigma_{\text{bulk}})$  could be noticed at temperatures  $>120$  °C, indicating a high temperature phase with lower activation energy. For exact determination, further investigations would have to be made.

Tab. 4.12: Bulk conductivities, activation energies and prefactors of 0.00-2.00 Ta-LLSO.

Composition	$\sigma_{\text{bulk}}$ at 20 °C [S·cm <sup>-1</sup> ]	$E_a$ [eV]	$\log(K)$ [s <sup>-1</sup> ]
0.00 Ta-LLSO	$2.58 \cdot 10^{-7}$	0.52(1)	2.36
0.25 Ta-LLSO	$5.37 \cdot 10^{-5}$	0.38(1)	2.95
0.50 Ta-LLSO	$7.56 \cdot 10^{-5}$	0.45(1)	3.82
0.75 Ta-LLSO	$7.94 \cdot 10^{-5}$	0.37(2)	3.38
1.00 Ta-LLSO	$3.53 \cdot 10^{-5}$	0.44(2)	3.94
1.25 Ta-LLSO	$9.39 \cdot 10^{-6}$	0.44(2)	3.98
1.50 Ta-LLSO	$6.38 \cdot 10^{-6}$	0.45(2)	3.65
1.75 Ta-LLSO	$1.78 \cdot 10^{-6}$	0.48(2)	3.51
2.00 Ta-LLSO	$6.62 \cdot 10^{-7}$	0.61(2)	4.16

For 0.00 Ta-LLSO in tetragonal modification, a bulk conductivity of  $\sigma_{\text{bulk}}=2.58 \cdot 10^{-7} \text{ S} \cdot \text{cm}^{-1}$  and an activation energy of 0.52(1) eV could be observed, showing similar results as found in the literature. [35] By increasing the amount of Ta, the bulk conductivity increases by two orders of magnitude to a maximum of  $\sigma_{\text{bulk}}=7.94 \cdot 10^{-5} \text{ S} \cdot \text{cm}^{-1}$  in 0.75 Ta-LLSO with an activation energy  $E_a$  of 0.37(2) eV. 0.50 Ta-LLSO shows comparable values regarding the bulk conductivity with an increased activation energy  $E_a$  of 0.45(1) eV. By further increasing the amount of Ta from 0.75-2.00 Ta-LLSO, the ionic conductivity decreases to  $6.62 \cdot 10^{-7} \text{ S} \cdot \text{cm}^{-1}$  and the activation energy  $E_a$  increases to 0.61(2) eV.

Taken all data into account, the best results could be observed for 0.75 Ta-LLSO with an ionic conductivity of  $7.94 \cdot 10^{-5} \text{ S} \cdot \text{cm}^{-1}$  and activation energy  $E_a$  of 0.37 eV. Further, it shows a relative shrinkage of 12.4 % and the density  $\rho$  is  $4.40 \text{ g} \cdot \text{cm}^{-3}$ .

## 4.3. Discussion

In the following subchapters, differences regarding the crystal structure and electrical properties between Ta-LLHO and Ta-LLSO will be discussed.

### 4.3.1. Crystal Structure

For the Ta-LLHO series, tetragonal 0.00 Ta-LLHO with SG  $I4_1/acd$  and cubic 0.25-2.00 Ta-LLHO with SG  $Ia\bar{3}d$  were synthesized. Compared to the Ta-LLHO series, the cubic modification in Ta-LLSO could be stabilized for 0.50-2.00 Ta-LLSO. For 0.00-0.25 Ta-LLSO, the tetragonal modification has formed.

The differences regarding the lattice parameter of cubic Ta-LLHO Ta-LLSO and Ta-LLZO, taken from reference [43], are displayed in Fig. 4.18.

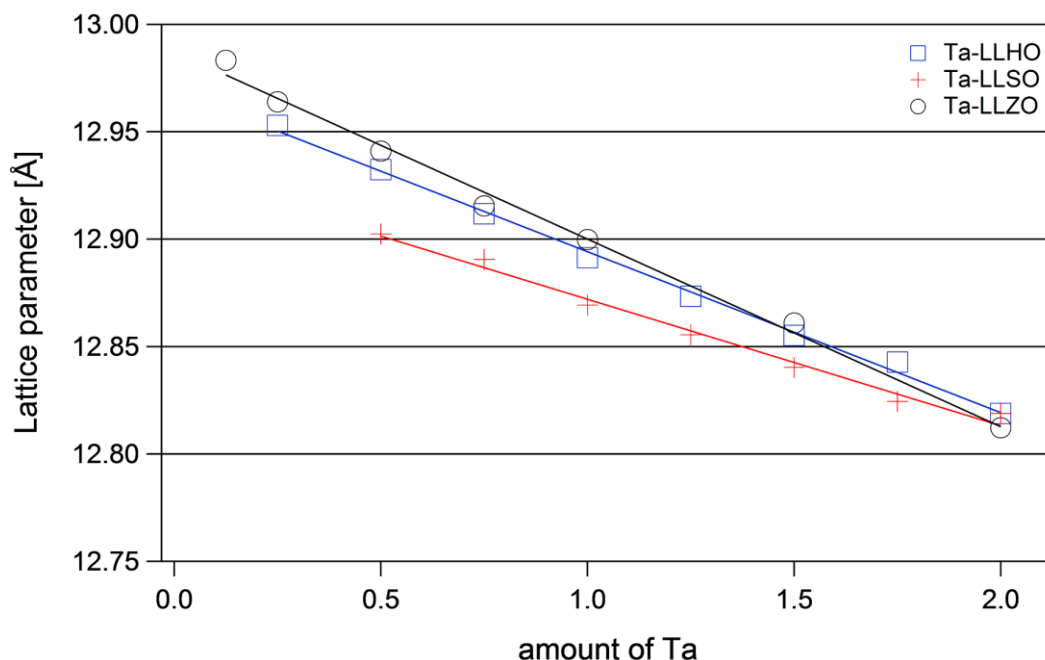


Fig. 4: Lattice parameter of Ta-LLHO, Ta-LLSO and Ta-LLZO, taken from reference [43]. The colored lines represent the fitting lines.

As seen in Fig 5.1, the lattice parameter of both series show linear decreasing values depending on the amount of Ta. Due to a higher ionic radius of Hf (85 pm) compared to Sn (83 pm), Ta-LLHO shows larger cell volumes with decreasing Ta compared to Ta-LLSO. For Ta-LLZO, analyzed by *Logéat et. al.* in 2012, a decreasing lattice parameter from approximately 12.983 Å to 12.812 Å for 0.125 to 2.00 Ta-LLZO were reported, showing comparable results as calculated in this diploma thesis. As well as for undoped LLHO and LLSO, the tetragonal modification was observed for undoped LLZO. [43]

The highest values for mean relative shrinkage were found for 1.00 Ta-LLHO (15.4 %) and 0.75 Ta-LLSO (12.4 %). However, no correlation between lattice parameter and densification could be found for both LLHO and LLSO series.

### 4.3.2. Electrochemical Studies

For the LLHO series, the highest bulk conductivities, measured at 20 °C, were found in 0.75-1.00 Ta-LLHO, with  $\sigma_{\text{bulk},0.75}=1.82 \cdot 10^{-4} \text{ S} \cdot \text{cm}^{-1}$  and  $\sigma_{\text{bulk},1.00}=1.93 \cdot 10^{-4} \text{ S} \cdot \text{cm}^{-1}$ . The corresponding activation energies are 0.461 eV and 0.466 eV. For the LLSO series, the highest bulk conductivity at 20 °C was determined for 0.75 Ta-LLSO with  $\sigma_{\text{bulk}}=7.94 \cdot 10^{-5} \text{ S} \cdot \text{cm}^{-1}$  and  $E_a=0.37 \text{ eV}$ , showing lower bulk conductivity than 0.75-1.00 Ta-LLHO, but also a lower activation energy (0.37 eV for 0.75 Ta-LLSO compared to 0.466 eV for Ta-LLHO). In Fig. 4.19, the a) bulk conductivity  $\sigma_{\text{bulk}}$ , the b) activation energy  $E_a$  and the c) prefactor  $K$  of both Ta-LLHO and Ta-LLSO are plotted vs. the amount of Ta.

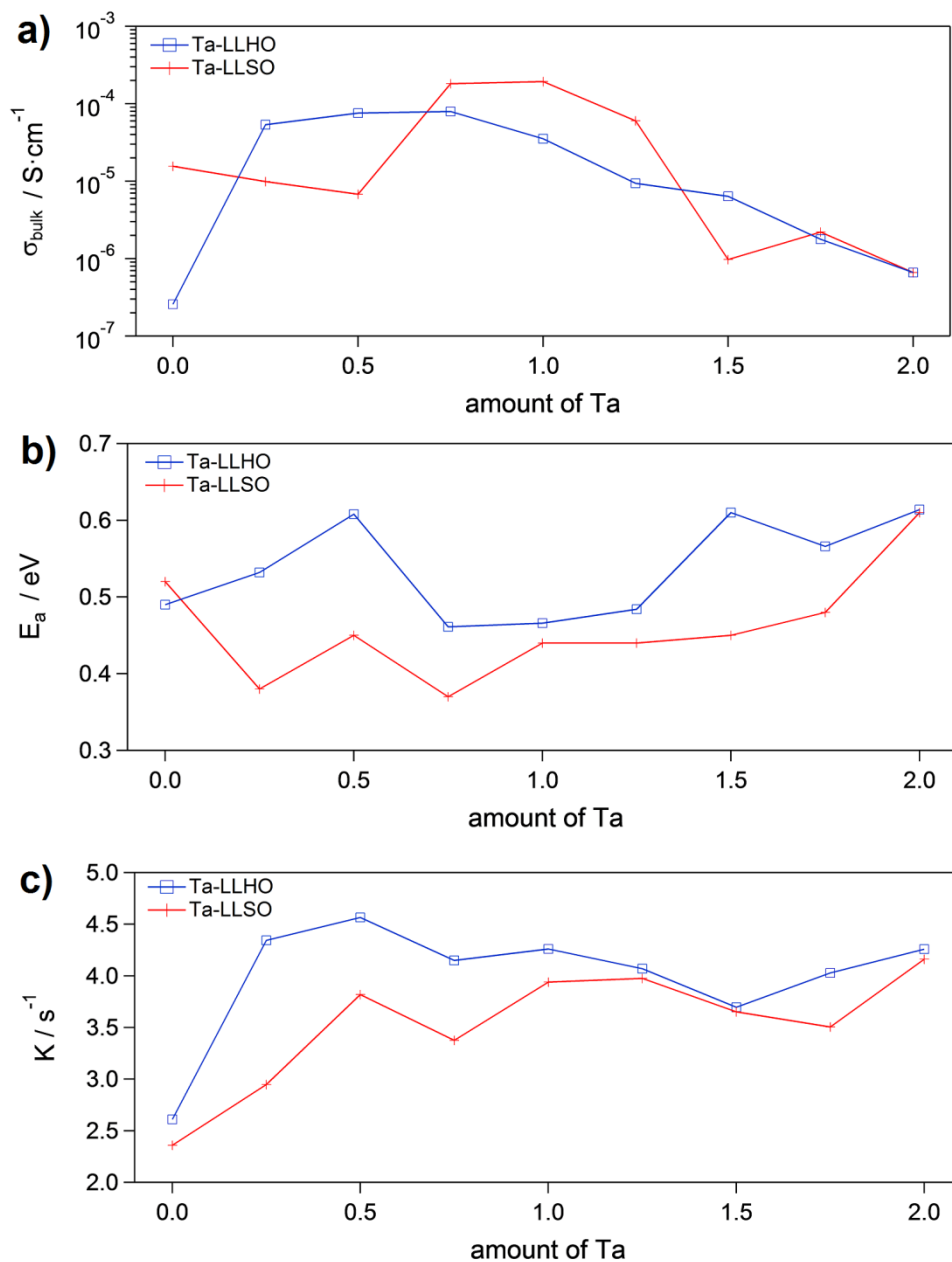


Fig. 4: Graphical representation of the a) bulk conductivity, the b) activation energy and c) prefactor of Ta-LLHO and Ta-LLSO.

1.00 Ta-LLHO as well as 0.75 Ta-LLSO show lower ionic conductivities than the best Ta doped LLZO, found in literature, which was found in 0.50 Ta-LLZO with  $\sigma=6.1 \cdot 10^{-4} \text{ S}\cdot\text{cm}^{-1}$ , observed at 27 °C, and an activation energy  $E_a$  of 0.40 eV.

## 5. Conclusion

$\text{Li}_{7-x}\text{La}_3\text{Hf}_{2-x}\text{Ta}_x\text{O}_{12}$  and  $\text{Li}_{7-x}\text{La}_3\text{Sn}_{2-x}\text{Ta}_x\text{O}_{12}$  garnets were successfully synthesized via solid state synthesis.

For the Ta-LLSO series, the tetragonal modification (SG:  $I4_1/acd$ ) could be found for  $x < 0.50$  Ta-LLSO. For  $x \geq 0.50$  Ta-LLSO, the cubic modification (SG:  $Ia\bar{3}d$ ) could be observed by using PXRD. A linear decreasing behavior of the lattice parameter from 12.90240 Å (0.50 Ta-LLSO) to 12.81884 Å (2.00 Ta-LLSO) could be determined. For the LLHO series, the tetragonal modification was obtained for  $x = 0.00$  and cubic modification for 0.25-2.00 Ta-LLHO. For 0.25 Ta-LLHO, a lattice parameter of 12.95294 Å could be determined, showing a linear decrease to 12.81884 Å for 2.00 Ta-LLHO.

Depending on the amount of Ta, a certain densification of both LLHO and LLSO series could be noticed with a maximum relative pellet shrinkage of 18.2 % determined for 1.00 Ta-LLHO and 15.2 % for 0.75 Ta-LLSO with mean densities  $\rho$  of 5.75 g·cm<sup>-3</sup> and 4.40 g·cm<sup>-3</sup>.

The analysis of the impedance spectroscopy data revealed two semicircles in the complex plane representation for tetragonal 0.00 Ta-LLHO and  $x < 0.5$  Ta-LLSO. By the calculation of the capacitance, these semiarcs could be assigned to grain boundary and bulk processes. For all other cubic samples, only one semicircle was observed, representing bulk processes. The Li-ion conductivity of LLHO increases from  $1.56 \cdot 10^{-6}$  S·cm<sup>-1</sup> to  $1.93 \cdot 10^{-4}$  S·cm<sup>-1</sup> with an increasing amount of Ta from 0.00 Ta atoms per formula unit (pfu) up to 1.00 Ta-LLHO, whereby the activation energy  $E_a$  remains similar with a value of about 0.48(1) eV. By further increasing the amount of Ta in the samples, yielding in  $\text{Li}_5\text{La}_3\text{Ta}_2\text{O}_{12}$ , the bulk conductivity  $\sigma_{\text{bulk}}$  decreases to  $6.62 \cdot 10^{-7}$  S·cm<sup>-1</sup> with an estimated activation energy  $E_a$  of 0.61 eV. For the LLSO series, 1.00 Ta-LLSO showed the highest ionic conductivity ( $7.94 \cdot 10^{-5}$  S·cm<sup>-1</sup> at 20 °C) with an activation energy  $E_a$  of 0.37 eV. Similar to the LLHO series, the conductivity decreases by further increasing the amount of Ta up to 2 Ta atoms pfu. This could be explained by the decreasing density of the samples as well as by the change of the charge carrier concentration as there are 6 Li atoms pfu in 1.00 Ta-LLHO and 6.25 Li atoms pfu in 0.75 Ta-LLSO, respectively, but only 5 Li atoms pfu in completely Ta doped LLHO and LLSO, respectively.

The next step will be testing the stability of all garnets by storing in air atmosphere and to check the electrochemical stability compared to differently doped Ta-LLZO. Further, tests will be performed in a symmetric Li-cell with the best samples of both series (1.00 Ta-LLHO and 0.75 Ta-LLSO). Lastly, doping with Al and Ga will be carried out to check if differently Ta doped LLHO and LLSO samples crystallize in the acentric cubic SG  $I - 43d$  (No. 220) similar to Ga-stabilized LLZO. [13]

# Bibliography

- [1] "Zukunftsentwicklungen." [Online]. Available: <http://www.zukunftsentwicklungen.de/welt.html>. [Accessed: 03-Oct-2018].
- [2] Ali, Khan, Chowdhury, Akhter, and Uddin, "Structural Properties, Impedance Spectroscopy and Dielectric Spin Relaxation of Ni-Zn Ferrite Synthesized by Double Sintering Technique," *Phys. Rev. Lett.*, vol. 93, no. 19, p. 196401, Nov. 2004.
- [3] M. Matsushita, K. Sato, T. Yoshiie, and Q. Xu, "Validity of Activation Energy for Vacancy Migration Obtained by Integrating Force&ndash;Distance Curve," *Mater. Trans.*, vol. 48, no. 9, pp. 2362–2364, 2007.
- [4] M. Duduta *et al.*, "Semi-solid lithium rechargeable flow battery," *Adv. Energy Mater.*, vol. 1, no. 4, pp. 511–516, 2011.
- [5] S. J. Visco, Y. S. Nimon, and B. D. Katz, "Protected Lithium Electrodes based on ceramic membranes," 8,778,522, 2014.
- [6] F. Chen, J. Li, Z. Huang, Y. Yang, Q. Shen, and L. Zhang, "Origin of the Phase Transition in Lithium Garnets," *J. Phys. Chem. C*, vol. 122, no. 4, pp. 1963–1972, 2018.
- [7] V. Thangadurai, S. Narayanan, and D. Pinzaru, "Garnet-type solid-state fast Li ion conductors for Li batteries: Critical review," *Chem. Soc. Rev.*, vol. 43, no. 13, pp. 4714–4727, 2014.
- [8] R. Guinebretière, *X-Ray Diffraction by Polycrystalline Materials*. 2013.
- [9] G. Hötzel and W. Weppner, "APPLICATION OF FAST IONIC CONDUCTORS IN SOLID STATE GALVANIC CELLS FOR GAS SENSORS," *Solid State Ionics*, vol. 19, pp. 1223–1227, 1986.
- [10] V. Accordingly and I. Boxes, *Principles of X-ray Diffraction*. 2006.
- [11] J. W. Morris, "Chapter 4 : Defects in Crystals," *Mater. Sci.*, pp. 76–107, 2007.
- [12] J. Awaka, N. Kijima, H. Hayakawa, and J. Akimoto, "Synthesis and structure analysis of tetragonal  $\text{Li}_7\text{La}_3\text{Zr}_2\text{O}_{12}$  with the garnet-related type structure," *J. Solid State Chem.*, vol. 182, no. 8, pp. 2046–2052, 2009.
- [13] D. Rettenwander *et al.*, "Structural and Electrochemical Consequences of Al and Ga Cosubstitution in  $\text{Li}_7\text{La}_3\text{Zr}_2\text{O}_{12}$  Solid Electrolytes," *Chem. Mater.*, vol. 28, no. 7, pp. 2384–2392, 2016.
- [14] J. Awaka, N. Kijima, H. Hayakawa, and J. Akimoto, "Synthesis and structure analysis of tetragonal  $\text{Li}_7\text{La}_3\text{Zr}_2\text{O}_{12}$  with the garnet-related type structure," *J. Solid State Chem.*, vol. 182, no. 8, pp. 2046–2052, Aug. 2009.
- [15] R. Wagner *et al.*, "Crystal Structure of Garnet-Related Li-Ion Conductor  $\text{Li}_{7-3x}\text{Ga}_x\text{La}_3\text{Zr}_2\text{O}_{12}$ : Fast Li-Ion Conduction Caused by a Different Cubic Modification?,"

- Chem. Mater.*, vol. 28, no. 6, pp. 1861–1871, 2016.
- [16] W. G. Zeier, “Structural limitations for optimizing garnet-type solid electrolytes: A perspective,” *Dalt. Trans.*, vol. 43, no. 43, pp. 16133–16138, 2014.
- [17] E. J. Cussen, “Structure and ionic conductivity in lithium garnets,” *J. Mater. Chem.*, vol. 20, no. 25, pp. 5167–5173, 2010.
- [18] R. Wagner *et al.*, “Synthesis, Crystal Structure, and Stability of Cubic  $\text{Li}_{7-x}\text{La}_3\text{Zr}_2\text{-xBi}_x\text{O}_{12}$ ,” *Inorg. Chem.*, vol. 55, no. 23, pp. 12211–12219, 2016.
- [19] R. D. Shannon, “Revised effective ionic radii and systematic studies of interatomic distances in halides and chalcogenides,” *Acta Crystallogr. Sect. A*, vol. 32, no. 5, pp. 751–767, 1976.
- [20] H. (Institut für M. U. M. G. Mehrer, *Diffusion in Solids*, vol. 155. 2007.
- [21] B.-O. Walter and H. Sowa, *Kristallographie*. 2013.
- [22] “slideplayer.com.” .
- [23] M. J. L. Sangster and A. M. Stoneham, “Calculation of absolute diffusion rates in oxides,” *J. Phys. C Solid State Phys.*, vol. 17, no. 34, pp. 6093–6104, 1984.
- [24] H. Toraya, “Introduction to X-ray analysis using the diffraction method,” *Rigaku J.*, vol. 32, no. 2, p. 2016.
- [25] V. Pecharsky and P. Zavalij, *Fundamentals of Powder Diffraction and Structural Characterization of Materials*. 2009.
- [26] E. P. Randviir and C. E. Banks, “Electrochemical impedance spectroscopy: An overview of bioanalytical applications,” *Anal. Methods*, vol. 5, no. 5, pp. 1098–1115, 2013.
- [27] E. Barsoukov and J. R. Macdonald, *Impedance Spectroscopy*. 2005.
- [28] M. Becherif and M. Benbouzid, “On impedance spectroscopy contribution to failure diagnosis in wind turbine generators,” *Int. J. Energy Convers.*, vol. 1, no. 3, pp. 147–153, 2013.
- [29] F. Preishuber-Pflügl and M. Wilkening, “Evidence of low dimensional ion transport in mechanosynthesized nanocrystalline  $\text{BaMgF}_4$ ,” *Dalt. Trans.*, vol. 43, no. 26, pp. 9901–9908, 2014.
- [30] T. Fir-mpd, “Reports 185,” *Science (80-. )*, no. August, pp. 676–681, 2008.
- [31] Z. Irshad, S. H. Shah, M. A. Rafiq, and M. M. Hasan, “First principles study of structural, electronic and magnetic properties of ferromagnetic  $\text{Bi}_2\text{Fe}_4\text{O}_9$ ,” *J. Alloys Compd.*, vol. 624, pp. 131–136, 2015.
- [32] W. Plieth, *Electrochemistry for Materials Science*. 2008.
- [33] Y. V. Baklanova *et al.*, “Synthesis and optical properties of cerium doped  $\text{Li}_7\text{La}_3\text{Hf}_2\text{O}_{12}$  with tetragonal garnet structure,” *J. Lumin.*, vol. 194, no. October 2017, pp. 193–199, 2018.

- [34] Y. V. Baklanova, L. G. Maksimova, T. A. Denisova, A. P. Tyutyunnik, and V. G. Zubkov, "Synthesis and luminescence properties of Tb<sup>3+</sup> and Dy<sup>3+</sup>-doped Li<sub>7</sub>La<sub>3</sub>Hf<sub>2</sub>O<sub>12</sub> with tetragonal garnet structure," *Opt. Mater. (Amst)*, no. February, pp. 0–1, 2018.
- [35] C. Deviannapoorani, S. Ramakumar, M. M. Ud Din, and R. Murugan, "Phase transition, lithium ion conductivity and structural stability of tin substituted lithium garnets," *RSC Adv.*, vol. 6, no. 97, pp. 94706–94716, 2016.
- [36] J. Awaka, N. Kijima, K. Kataoka, H. Hayakawa, K. Ichi Ohshima, and J. Akimoto, "Neutron powder diffraction study of tetragonal Li<sub>7</sub>La<sub>3</sub>Hf<sub>2</sub>O<sub>12</sub> with the garnet-related type structure," *J. Solid State Chem.*, vol. 183, no. 1, pp. 180–185, 2010.
- [37] M. B. Labhane and P. Palsodkar, "Various architectures of analog to digital converter," *2015 Int. Conf. Commun. Signal Process. ICCSP 2015*, pp. 1199–1203, 2015.
- [38] Y. V. Baklanova *et al.*, "Stabilization of cubic Li<sub>7</sub>La<sub>3</sub>Hf<sub>2</sub>O<sub>12</sub> by Al-doping," *J. Power Sources*, vol. 391, no. December 2017, pp. 26–33, 2018.
- [39] J. T. S. Irvine, D. C. Sinclair, and A. R. West, "Electroceramics: Characterization by Impedance Spectroscopy," *Adv. Mater.*, vol. 2, no. 3, pp. 132–138, 1990.
- [40] S. Narayanan, F. Ramezanipour, and V. Thangadurai, "Enhancing Li ion conductivity of garnet-type Li<sub>5</sub>La<sub>3</sub>Nb<sub>2</sub>O<sub>12</sub> by Y- and Li-codoping: Synthesis, structure, chemical stability, and transport properties," *J. Phys. Chem. C*, vol. 116, no. 38, pp. 20154–20162, 2012.
- [41] X. Qian, N. Gu, Z. Cheng, X. Yang, E. Wang, and S. Dong, "Methods to study the ionic conductivity of polymeric electrolytes using a.c. impedance spectroscopy," *J. Solid State Electrochem.*, vol. 6, no. 1, pp. 8–15, 2001.
- [42] A. R. West, *Solid State Chemistry and its Applications*. 1984.
- [43] A. Logéat *et al.*, "From order to disorder: The structure of lithium-conducting garnets Li<sub>7-x</sub>La<sub>3</sub>TaxZr<sub>2-x</sub>O<sub>12</sub> (x = 0–2)," *Solid State Ionics*, vol. 206, pp. 33–38, 2012.

# List of Figures

Fig. 1.1: Schematic representation of tetragonal LLZO. $\text{La}(1)\text{O}_8$ and $\text{La}(2)\text{O}_8$ are dodecahedrons and $\text{ZrO}_6$ represents a octahedron. Li sits on tetrahedral 8a and octahedral 16f and 32g, respectively. The reference is taken from [12].	3
Fig. 1.2: Schematic representation of a) cubic LLZO with SG $Ia\bar{3}d$ and b) corresponding diffusion pathway. Red spheres represent the tetrahedrally coordinated (24d) sites. $\text{Zr}^{4+}$ occupies the 16a octahedra (green) and $\text{La}^{3+}$ the 24c dodecahedra (blue). The figure is taken from reference [13].	4
Fig. 2.1: Mechanism of the vacancy diffusion. The blue points represent the matrix of the crystal lattice, the green circle the jumping particle before (left) and after (right) migration. The figure is taken from reference [22].	8
Fig. 2.2: Mechanism of the interstitial diffusion. The blue points represent the matrix of the crystal lattice, the orange circle the jumping particle before (left) and after (right) migration. The figure is taken from reference [22].	9
Fig. 2.3: Schematic representation of vacancy migration. The white points represent the matrix of the crystal lattice; the grey circle is the jumping particle. $E_m$ shows the energy difference between the activated and ground state. The figure is taken from reference [3].	9
Fig. 2.4: Representation of Schottky- (a) and Frenkel (c) defect in comparison to an ideal crystal lattice (b). Circles with a '+' represent cations, circles with '-' show anions. Vacancies are represented by squares. The figure was taken from reference [21].	11
Fig. 2.5: Graphical representation of Bragg's law. $\theta$ denotes the angle of the incident and diffracted X-ray beam, $d_{hkl}$ is the distance between the lattice planes ( $hkl$ ). The figure is taken from reference [25].	13
Fig. 2.6: Sinusoidal current response in a (pseudo)-linear system. The figure is taken from reference [28].	15
Fig. 2.7: Graphical representation of a typical conductivity isotherm. The blue lines give an optical separation of the curve in four regions.	17
Fig. 2.8: a) Equivalent circuit with electrolyte resistance $R_{el}$ and capacitance $C_{dl}$ in series. b) Schematic representation of a Nyquist plot for $-Z''$ vs. $Z'$ as a function of the frequency $\omega$ in serial connection.	19
Fig. 2.9: a) Equivalent circuit with $R_{el}$ , $R_{ct}$ and $C_{dl}$ in parallel connection. b) Schematic representation of a Nyquist plot for $-Z''$ vs. $Z'$ as a function of the frequency $\omega$ in parallel connection.	19
Fig. 3.1: Setup for calcination.	21
Fig. 3.2: Temperature program of the calcination process.	22

Fig. 3.3: Setup for the sintering process. ....	23
Fig. 3.4: General temperature program of the sintering process. ....	23
Fig. 4.1: Results of the DTA-TG measurement of the calcinated undoped LLHO sample. The arrows point to the onset and offset temperatures in the TG (black lines). The dashed lines denote the exothermic areas of the DTA (blue line). ....	26
Fig. 4.2: X-ray powder pattern of 0.00 Ta-LLHO heat treated at various temperatures and holding times between 980 °C und 1230 °C with and without milling, prepared in air atmosphere. The blue dotted lines mark secondary phases. The reference was taken from the ICSD database and is used for comparison. ....	28
Fig. 4.3: X-ray diffraction powder pattern of 0.00-2.00 Ta-LLHO series. References #68252 (cubic LLTO) and #174202 (tetragonal LLHO) were taken from ICSD database. ....	29
Fig. 4.4: Lattice parameter in dependency of Ta content in 0.25-2.00 Ta-LLHO. The blue line represents the fitting line with $R^2=0.997$ . ....	30
Fig. 4.5: Graphical representation of the density (blue squares) and relative shrinkage (black dots) of Ta-LLSO at different compositions. The error bars mark the standard deviation. ....	32
Fig. 4.6: Conductivity isotherms of 0.00 Ta-LLHO, sintered at 1100 °C for 24 h. $\sigma'$ is plotted vs. $\nu$ in the heating process of 0.00 Ta-LLHO. The red dotted line represents a $\sigma_{DC}$ -plateau. ....	33
Fig. 4.7: Nyquist diagrams of a) polycrystalline 0.00 Ta-LLHO and b) cubic 1.00 Ta-LLHO measured at 20 °C. The red, dashed lines represent the fitted semicircles, observed by EIS measurements. The red arrows point to the intercept with the $Z'$ -axis and the black arrows mark the maxima of the semicircles and to the area, where EP takes place, respectively. ...	34
Fig. 4.8: Arrhenius plot of the bulk and GB process of 0.00 Ta-LLHO, calculated from the conductivity at the intercept with $Z'$ -axis of the semicircle. The black and red lines represent the fitting lines, which were used for the determination of the activation energies $E_a$ . ....	36
Fig. 4.9: Arrhenius plots of 0.00-2.00 Ta-LLHO. The lines between the dots serve as guides to the eye. ....	36
Fig. 4.10: Results of the DTA-TG measurement of the calcinated, undoped LLSO sample. The arrows point to the onset and offset temperatures in the TGA (black lines). The dashed lines denote the exothermic areas of the DTA (blue line). ....	39
Fig. 4.11: X-ray powder pattern of 0.00 Ta-LLSO heat treated at various temperatures and holding times between 850 °C and 1230 °C with and without milling, prepared in air atmosphere. The blue dotted lines mark secondary phases. The references were taken from the ICSD database and are used for comparison. ....	41
Fig. 4.12: X-ray diffraction pattern of 0.00-2.00 Ta-LLSO series. The blue dotted lines represent secondary phases. References #68252 (cubic LLTO) as well as #237808 (cubic modification) and #163914 (tetragonal modification) were taken from ICSD database. ....	42

Fig. 4.13: Lattice parameters in dependency of Ta content in 0.50-2.00 Ta-LLSO. The red line represents the fitting line with $R^2=0.988$ . .....	43
Fig. 4.14: Graphical representation of the density (red squares) and relative shrinkage (black dots) of Ta-LLSO at different compositions. The error bars mark the standard deviation. ...	45
Fig. 4.15: Real part of the conductivity $\sigma'$ vs. the frequency $\nu$ of 0.00 Ta-LLSO at selected temperatures. The red line represents a $\sigma_{DC}$ -plateau. ....	46
Fig. 4.16: Nyquist plots of a) polycrystalline 0.00 Ta-LLSO and b) cubic 1.00 Ta-LLSO measured at 20 °C. The red, dashed lines represent the fitted semicircles, observed by EIS measurements. The red arrows point to the intercept with the $Z'$ -axis and the black arrows mark the maxima of the semicircles and to the area, where EP takes place, respectively. ...	47
Fig. 4.17: Arrhenius diagram of the 0.00-2.00 Ta-LLSO samples. The lines between the dots serve as guides to the eye. ....	48
Fig. 4.18: Lattice parameter of Ta-LLHO, Ta-LLSO and Ta-LLZO, taken from reference [43]. The colored lines represent the fitting lines. ....	50
Fig. 4.19: Graphical representation of the a) bulk conductivity, the b) activation energy and c) prefactor of Ta-LLHO and Ta-LLSO. ....	51

# List of Tables

Tab. 1.1: Description of the garnet structure. The reference is taken from [8].	2
Tab. 1.2: Ionic radii of Hf, Sn and Ta, taken from reference [19].	5
Tab. 3.1: Composition of the Ta doped LLHO.	21
Tab. 3.2: General pellet dimensions.	23
Tab. 3.3: Composition of the Ta doped LLSO.	24
Tab. 4.1: Used temperatures and holding times in the sintering process for each LLHO sample.	28
Tab. 4.2: Calculated unit cell parameters of 0.00 - 2.00 Ta-LLHO.	30
Tab. 4.3: Optical change of 0.00-2.00 Ta-LLHO after sintering.	31
Tab. 4.4: Relative shrinkage of 0.00-2.00 Ta-LLHO after sintering.	31
Tab. 4.5: Mean density of 0.00-2.00 Ta-LLHO after sintering.	32
Tab. 4.6: Calculated bulk conductivities and activation energies of 0.00-2.00 Ta-LLHO.	37
Tab. 4.7: Used temperatures and holding times in the sintering process for each LLSO sample.	40
Tab. 4.8: Lattice parameter of 0.00-2.00 Ta-LLSO.	43
Tab. 4.9: Optical change of 0.00-2.00 Ta-LLSO after sintering.	44
Tab. 4.10: Relative shrinkage of 0.00-2.00 Ta-LLSO after sintering.	44
Tab. 4.11: Mean density of 0.00-2.00 Ta-LLSO after sintering.	45
Tab. 4.12: Bulk conductivities, activation energies and prefactors of 0.00-2.00 Ta-LLSO.	48